Rep. Prog. Phys. 55 (1992) 599–651. Printed in the UK

Surface x-ray diffraction

I K Robinson†§ and D J Tweet‡||

† AT&T Bell Laboratories, Murray Hill, NJ 07974, USA
‡ Department of Physics, University of Washington, Seattle, WA 98195, USA

Abstract

A general introduction to x-ray diffraction and its application to the study of surfaces and interfaces is presented. The application of x-ray diffraction to various problems in surface and interface science is illustrated through five different techniques: crystal truncation rod analysis, two-dimensional crystallography, three-dimensional structure analysis, the evanescent wave method and lineshape analysis. These techniques are explained with numerous examples from recent experiments and with the aid of an extensive bibliography.

This review was received in October 1991.

§ Address from August 1992: Department of Physics, University of Illinois, Urbana, IL 61801,USA.
|| Present address: NEC Fundamental Research Laboratories, 34 Miyukigaoka, Tsukuba, Ibaraki 305, Japan.

0034-4885/92/050599+53$18.00

Contents

1. Introduction

The purpose of this review is to discuss some different ways in which x-ray diffraction is used to study surfaces and interfaces. We begin with an elementary discussion of the theory of diffraction, starting with the scattering from a single electron. From there the idea of reciprocal space is derived, a concept used in most thinking about diffraction measurements. Next, these general concepts are applied to the special case of surfaces. This sets the stage for the main focus of this review: five specific diffraction techniques used to study two-dimensional structures, and illustrated with results from recent experiments on actual surfaces and interfaces.

Surface science is a subject that has grown enormously in the last decade, partly because of the availability of new electron-based tools. X-ray diffraction has contributed also to many advances in the field, particularly when synchrotron radiation is used: satisfactory signal levels are obtained for surfaces of all but the lightest elements. Previous reviews of x-ray diffraction from surfaces were made by Feidenhans'l (1989), Fuoss and Brennan (1990) and Robinson (1991).

Interface science, on the other hand, is still in its infancy as far as structural analysis is concerned. Relatively crude techniques, such as dissolution or erosion of one half of an interface, exist but have limited application. A central point of this review is that surfaces and interfaces can be treated more or less interchangeably from the point of view of x-ray diffraction. It is expected that in the coming decade considerable use of these techniques will occur and that, by the end of the decade, interfacial processes such as crystal growth, epitaxy, interfacial bonding, wetting, roughening and adhesion will be understood far better at the atomic scale.

2. X-ray diffraction background

In this section we calculate what happens when x-rays are directed at a crystal and the scattered rays are viewed from various angles a large distance away. Specifically, we calculate the cross section of scattering from the sample. X-rays are used because their wavelength is comparable with the interatomic spacing. To better understand the scattering formulae, we will build the crystal in stages, starting from one electron. Figure 1 defines the real and reciprocal space vectors which are used in deriving the scattering formulae below. The Thompson formula (Warren 1969, Jackson 1975) describes the amplitude of the wave A_1 that comes from a scattering electron at $\boldsymbol{r}_e$, as a function of the amplitude of the wave A_0 that goes in, assuming the dipole approximation,

$$A_1 \exp(-i\boldsymbol{k}_f \cdot \boldsymbol{r}_e) = A_0 \frac{e^2}{mc^2} \frac{1}{R_0} \exp(-i\boldsymbol{k}_i \cdot \boldsymbol{r}_e) \tag{1}$$

where e and m are the electron's charge and mass, and R_0 is the distance to the observer. $1/R_0$ arises because a spherical wave comes out when a plane wave goes

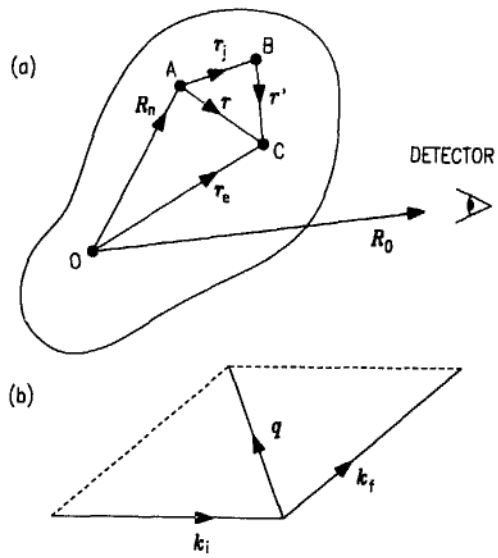

Figure 1. (*a*) Definition of the real space vectors used in equations (1)–(10). Point O is the origin of the crystal, point A is the origin for the nth unit cell, point B is the jth atom of the nth unit cell and point C is an electron belonging to the jth atom of the nth unit cell. (*b*) Definition of the reciprocal space incident and exit wave vectors $\boldsymbol{k}_i$ and $\boldsymbol{k}_f$. These wave vectors both have magnitude $2\pi/\lambda$, with λ being the x-ray wavelength. The momentum transfer $\boldsymbol{q}$ is $\boldsymbol{k}_f - \boldsymbol{k}_i$.

in. The constant, e^2/mc^2, has a very small value, of 3×10^{-15} m. Thus, even with the large number of electrons in a crystal, the total scattering cross section is still quite small. Consequently, the kinematical approximation is valid, in which the amplitude scattered by an object is taken to be the sum of independent contributions from all the individual electrons.

2.1. Momentum transfer

A very important concept, the 'momentum transfer', is now introduced, as shown in figure 1(*b*). $\boldsymbol{q}$ is the vector difference between the ingoing wavevector $\boldsymbol{k}_i$ and the outgoing wavevector $\boldsymbol{k}_f$. Since $|\boldsymbol{k}_i| = |\boldsymbol{k}_f| = |\boldsymbol{k}| = (2\pi/\lambda)$ for elastic scattering, where λ is the x-ray wavelength, we can immediately derive the Bragg law,

$$|\boldsymbol{q}| = 2|\boldsymbol{k}| \sin \frac{2\theta}{2}. \tag{2}$$

The momentum transfer is the fundamental experimental variable. It relates both to the experimental scattering angle, 2θ, through equation (2), and to the theoretical scattering amplitude that is derived below. This can be seen by rearranging equation (1), with the definition $\boldsymbol{q} \equiv \boldsymbol{k}_f - \boldsymbol{k}_i$,

$$A_1 = A_0 \frac{e^2}{mc^2} \frac{1}{R_0} \exp(i\boldsymbol{q} \cdot \boldsymbol{r}_e). \tag{3}$$

The results of a scattering experiment may be thought of as a map in momentum space, where $\boldsymbol{q}$ is the independent variable and the scattered intensity is the dependent variable. In general, the sample has three degrees of orientational freedom, and the

scattering angle makes a fourth, so an instrument called a four-circle diffractometer is used. This has four concentric circular motions, three of which, called ω, ϕ and χ, move the sample to the particular direction of q, and one that moves the detector by an angle 2θ, setting the magnitude of q. In practice, the orientation of the sample, position of the detector, and counting of the scattered x-ray photons are all computer controlled.

We now have the x-ray scattering amplitude from an individual electron, equation (3). Using the kinematical approximation, by simply summing the scattering amplitude from each electron, we arrive first at the scattering from an individual atom, then from one unit cell of the crystal, and finally from the entire macroscopic crystal.

2.2. *Form and structure factors*

In summing the scattering amplitudes from each electron in an atom, it is necessary to represent the electrons by their density distributions, as described by their wavefunctions. This summation then becomes an integration:

$$A_2 = A_0 \frac{e^2}{mc^2} \frac{1}{R_0} \int_{-\infty}^{+\infty} \rho(\boldsymbol{r}') \exp(\mathrm{i}\boldsymbol{q} \cdot (\boldsymbol{R}_n + \boldsymbol{r}_j + \boldsymbol{r}')) \, \mathrm{d}^3 r'$$

$$= A_0 \frac{e^2}{mc^2} \frac{1}{R_0} f(q) \exp(\mathrm{i}\boldsymbol{q} \cdot (\boldsymbol{R}_n + \boldsymbol{r}_j)) \tag{4}$$

where

$$f(q) = \int_{-\infty}^{+\infty} \rho(\boldsymbol{r}') \exp(\mathrm{i}\boldsymbol{q} \cdot \boldsymbol{r}') \, \mathrm{d}^3 r'. \tag{5}$$

The atomic form factor, $f(q)$, is defined as the Fourier transform of the electron density for a single atom. The atomic form factor is written as a function of the magnitude of the momentum transfer, independent of direction, because in almost all cases the atom is spherically symmetric. More strictly, $f(q)$ is a complex number and somewhat energy dependent because the x-ray can excite atomic transitions. $f(q)$ is a tabulated function for all atoms in the periodic table.

The third step of the assembly is to add up the atoms inside one unit cell of the crystal. The atoms may not all be the same chemical element so they must be distinguished by assigning separate form factors, $f_j(q)$. If there are N_c atoms in the unit cell, then

$$A_3 = A_0 \frac{e^2}{mc^2} \frac{1}{R_0} \sum_{j=1}^{N_c} f_j(q) \exp(\mathrm{i}\boldsymbol{q} \cdot (\boldsymbol{R}_n + \boldsymbol{r}_j))$$

$$= A_0 \frac{e^2}{mc^2} \frac{1}{R_0} F(\boldsymbol{q}) \exp(\mathrm{i}\boldsymbol{q} \cdot \boldsymbol{R}_n) \tag{6}$$

where

$$F(\boldsymbol{q}) = \sum_{j=1}^{N_c} f_j(q) \exp(\mathrm{i}\boldsymbol{q} \cdot \boldsymbol{r}_j). \tag{7}$$

Once again, we use a simplifying notation, calling the function $F(q)$, the sum over all the atoms within one unit cell, the structure factor. Now, of course, $F(q)$ depends on the direction of q as well as the magnitude because the relative positions of the atoms in space are important. Here the structure factor is defined in terms of the atomic form factors, $f_j(q)$. Alternatively, it is sometimes convenient to think of $F(q)$ in terms of $\rho(r)$, the electron density of one unit cell, where r is defined as in figure 1. Defining $\rho(r)$ as the sum of the contributions from all the atoms in the unit cell,

$$\rho(r) = \sum_{j=1}^{N_c} \rho_j(r - r_j) \tag{8}$$

the structure factor can be written as

$$F(q) = \int \rho(r) \exp(iq \cdot r)\, d^3r. \tag{9}$$

This is an alternative, but equivalent, definition of the structure factor: the Fourier transform of the electron density for one unit cell of the crystal.

2.3. 3D diffraction

The final step is to add up all the unit cells to make the whole crystal. This is where the scattering becomes strongly focused into beams along certain directions and is then called diffraction. For simplicity, assume the crystal to be block-shaped with N_1, N_2 and N_3 unit cells along the three crystal axes defined by the vectors, a_1, a_2 and a_3. We add up phase factors for the positions of the origin of each unit cell, $R_n = n_1a_1 + n_2a_2 + n_3a_3$,

$$A_4 = A_0 \frac{e^2}{mc^2} \frac{1}{R_0} F(q) \sum_{n_1=0}^{N_1-1} \sum_{n_2=0}^{N_2-1} \sum_{n_3=0}^{N_3-1} \exp(iq \cdot (n_1a_1 + n_2a_2 + n_3a_3)). \tag{10}$$

This is simply a geometric sum, because we have already isolated all the chemistry inside the structure factor. What is left can be written down explicitly and is the same for all crystals.

Let us examine one of the sums that appears in equation (10) more closely. From this we will derive all of the important properties of diffraction, including diffraction from surfaces. Define the function

$$\begin{aligned} S_N(x) &= \sum_{n=0}^{N-1} \exp(ixn) \\ &= \frac{1 - \exp(ixN)}{1 - \exp(ix)}. \end{aligned} \tag{11}$$

This complex quantity, with $x = qa$, represents a simplified version of the scattering amplitude for a one-dimensional crystal containing N atoms. The quantity of interest to experimenters is the square modulus of S, representing the scattered intensity:

$$|S_N(x)|^2 = \frac{\sin^2(Nx/2)}{\sin^2(x/2)}. \tag{12}$$

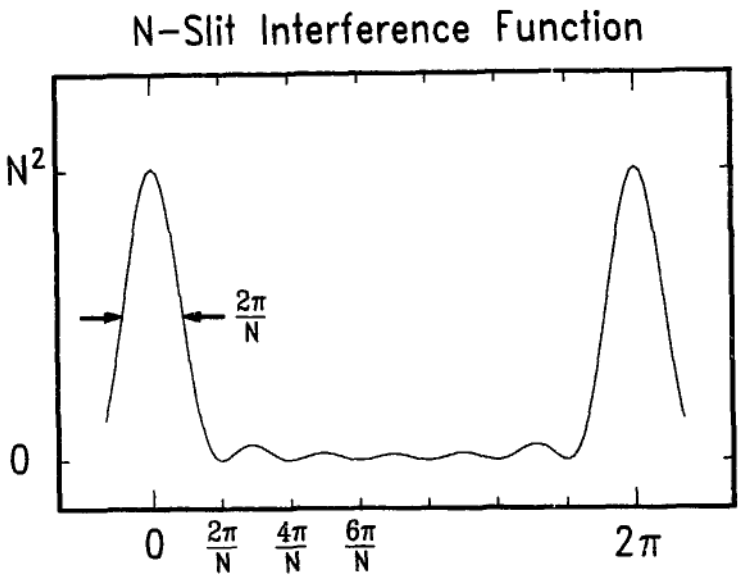

Figure 2. N-slit interference function shown here for N=6. Note that the primary maxima are spaced 2π apart in units of $\boldsymbol{q}\cdot\boldsymbol{a}_3$ while the subsidiary maxima are spaced $2\pi/N$ apart. Thus there are $N-2$ subsidiary maxima between each pair of primary maxima and from the spacing of the subsidiary maxima the value of N can be deduced.

This is called the 'N-slit interference function' because of its use in optics. It is plotted in figure 2.

We can now write the diffracted amplitude as a product of slit functions,

$$A_4 = A_0 \frac{e^2}{mc^2}\frac{1}{R_0}F(\boldsymbol{q})S_{N_1}(\boldsymbol{q}\cdot\boldsymbol{a}_1)S_{N_2}(\boldsymbol{q}\cdot\boldsymbol{a}_2)S_{N_3}(\boldsymbol{q}\cdot\boldsymbol{a}_3). \tag{13}$$

For the time being, we will consider the large-N limit of the N-slit function, corresponding to the case of a large crystal. $S_N(qa)$ is sharply peaked at $q = 2\pi m/a$ where m is an integer, and tends in the limit to a periodic array of δ functions with a spacing of $2\pi/a$. This tells us that the diffracted intensity from a crystal has the special property of being only along specific, well-defined directions.

The generalization to three dimensions (3D) of this statement leads to the concept of a reciprocal lattice. The diffracted intensity is the product of three orthogonal, periodic δ-function arrays, so we can write down three separate conditions that have to be met simultaneously for the intensity to be at a maximum:

$$\begin{aligned}\boldsymbol{q}\cdot\boldsymbol{a}_1 &= 2\pi h\\ \boldsymbol{q}\cdot\boldsymbol{a}_2 &= 2\pi k\\ \boldsymbol{q}\cdot\boldsymbol{a}_3 &= 2\pi l.\end{aligned} \tag{14}$$

These three equations, all of which have to be true for diffraction to take place, are called the Laue conditions. The integers h, k and l are called Miller indices. The three conditions can be simultaneously satisfied by the vector

$$\boldsymbol{q} = h\boldsymbol{b}_1 + k\boldsymbol{b}_2 + l\boldsymbol{b}_3 \tag{15}$$

with

$$\boldsymbol{b}_1 = 2\pi\frac{\boldsymbol{a}_2\times\boldsymbol{a}_3}{\boldsymbol{a}_1\cdot\boldsymbol{a}_2\times\boldsymbol{a}_3} \tag{16}$$

etc.

Since an arbitrary set of integers h, k and l gives us a q that satisfies the Laue conditions, the allowed values themselves form a 3D lattice of points. This 'reciprocal lattice' is spanned by the vectors b_1, b_2 and b_3 which are orthogonal to the a_1, a_2 and a_3 that span the diffracting crystal. The $\{a_j\}$s have units of length (Å), so the $\{b_j\}$s have units of inverse length (Å^{-1}). For further discussion of the properties of the reciprocal lattice, the reader is referred to one of the many excellent texts on crystallography (Lipson and Cochran 1966).

Now we understand the diffraction pattern of a 3D crystal: the diffracted intensity is zero except at discrete points that lie on a lattice in the space of the momentum transfer vector, q. When we measure the intensity at such a hkl point, it is given by

$$I_{hkl} = \left| A_0 \frac{e^2}{mc^2} \frac{1}{R_0} F(hb_1 + kb_2 + lb_3) N_1 N_2 N_3 \right|^2 . \tag{17}$$

3. Surface diffraction

Up to this point we have considered diffraction quite generally; with figure 3 we introduce the special case of diffraction from a surface. We really have to consider two cases: figure 3(a) is the case of an ideal two-dimensional (2D) monolayer, hard to realize in nature; the other is the case of figure 3(b) that most surface scientists really talk about implicitly, the case of a truncated 3D crystal. The top layer could have a structure of its own, or it could be a simple continuation of the bulk, with slight modifications.

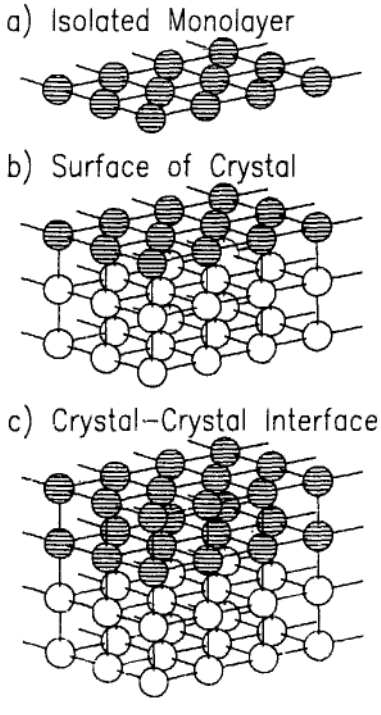

Figure 3. Schematic pictures illustrating 2D layers existing at surfaces and interfaces. (a) Isolated monolayer, (b) surface of crystal, (c) crystal–crystal interface.

It is also possible to include *two* bulk media in the problem, one on each side of an interface, as figure 3(*c*) shows. Either one or both media may be crystalline. The diffraction formulae we derive below apply to these situations equally well.

The diffraction from all three cases can be described using equation (13). If we take $\boldsymbol{a}_3$ to be along the surface normal, the isolated monolayer is handled by setting $N_3 = 1$. The diffraction is then independent of $\boldsymbol{q} \cdot \boldsymbol{a}_3$, the component of momentum transfer perpendicular to the surface. In 3D reciprocal space, we find the diffraction is a 2D lattice of rods, as shown in figure 4(*a*). Each rod is a line of scattering which is sharp in both directions parallel to the surface and diffuse (or continuous) in the out-of-plane direction. These rods are the chief characteristic of diffraction from surfaces.

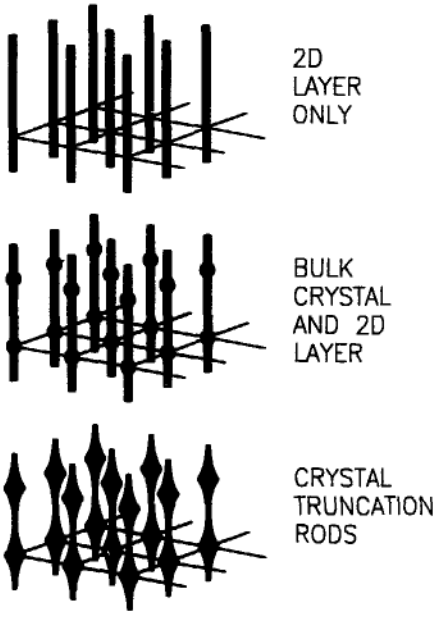

Figure 4. Schematic diffraction patterns corresponding to figure 3. (*a*) For the isolated monolayer, (*b*) for the surface of a 3D crystal, (*c*) more realistic representation showing variation of intensity along crystal truncation rods (CTRs).

In our experiment, if we were to measure at any point along one of these reciprocal space rods, we would always obtain some intensity, but if we measured in between them we would measure nothing because of the in-plane δ function. The usual form of presentation of such data is in the form of a *scan* or linear slice through space cutting across one of these features. Notice that we always talk about measurements in reciprocal space: this is the language that is always used in crystallography and diffraction physics. We think in the space of the reciprocal lattice, not in the real space of the crystal itself. Since what we measure is the scattering at various diffractometer angles, we are, in effect, making a map of reciprocal space. It is, therefore, extremely convenient to think in these terms. Furthermore, many aspects of the physics of crystals are greatly simplified when viewed in reciprocal space, as will be evident later on from the examples.

3.1. Crystal truncation rods

Figure 4(*b*) is the diffraction from the structure of figure 3(*b*) with a 2D layer plus the bulk. We have simply superimposed the two diffraction patterns of the surface (lines) and the bulk (dots) on top of each other. This picture conveys the idea that the Bragg rods of diffraction due to the surface pass through the Bragg points of the bulk. The rods, however, are by no means flat in their intensity profiles as they were for the monolayer case, and in fact they look more like the schematic representation of figure 4(*c*). This is because all layers of the crystal contribute. The intensity profile can be derived by detailed consideration of the N-slit function, equation (12). The numerator, $\sin^2(N\boldsymbol{q}\cdot\boldsymbol{a}_3/2)$, is an extremely rapidly varying function of q, at least for large N, and is in any case smeared out in a real experiment because of finite resolution; since it is always positive, we can approximate it by its average value of $\frac{1}{2}$. This gives a simpler form for the limit of large N that is actually independent of N,

$$|S'(\boldsymbol{q}\cdot\boldsymbol{a}_3)|^2 = \frac{1}{2\sin^2(\boldsymbol{q}\cdot\boldsymbol{a}_3/2)}. \tag{18}$$

Although this approximation is not useful at any of the Bragg points given by the third Laue condition (equation (14)), $\boldsymbol{q}\cdot\boldsymbol{a}_3 = 2\pi l$, it tells us that the intensity in between them is actually non-zero along the surface normal.

Such rods are called 'crystal truncation rods' (CTRs) since they arise from the crystal being truncated (Robinson 1986). They have the characteristic dependence on perpendicular momentum transfer as given by equation (18) and plotted in figure 5. The origin of this intensity variation along the rod can also be seen by constuction of the diffraction amplitude coming from the semi-infinite crystal inside $z \leqslant 0$ with absorption ϵ from one layer to the next,

$$\begin{aligned} S''(\boldsymbol{q}\cdot\boldsymbol{a}_3) &= \sum_{j=0}^{\infty} \exp(-(\mathrm{i}\boldsymbol{q}\cdot\boldsymbol{a}_3 + \epsilon)j) \\ &= \frac{1}{1-\exp(-\mathrm{i}\boldsymbol{q}\cdot\boldsymbol{a}_3 - \epsilon)}. \end{aligned} \tag{19}$$

In the limit of ϵ tending to zero, the square modulus of $S''(\boldsymbol{q}\cdot\boldsymbol{a}_3)$ tends to the form given in equation (18) above for $S'(\boldsymbol{q}\cdot\boldsymbol{a}_3)$. When ϵ is small, corresponding to the real case of an absorbing crystal, equation (19) is only significantly different from the ideal case of equation (18) at and very close to the Bragg peaks. We know equation (18) must be incorrect for real crystals because it predicts an *infinite* value for the intensity at the Bragg peaks: for complete fidelity we must introduce both the effects of absorption and the full dynamical theory.

It is important to make the distinction between the truncation rods, passing through bulk reciprocal lattice points, and those due to an isolated monolayer. Both can exist together in the same sample because an adsorbed layer does not necessarily have to be registered with the crystal underneath. In the interesting case of reconstructed surfaces, the outer layer(s) of a crystal spontaneously rearrange to produce a new periodicity (see below). For the diffraction of the added layer not to pass through the bulk Bragg points, however, it must have a different periodicity. The analysis of these two kinds of rod differ somewhat, as we shall see.

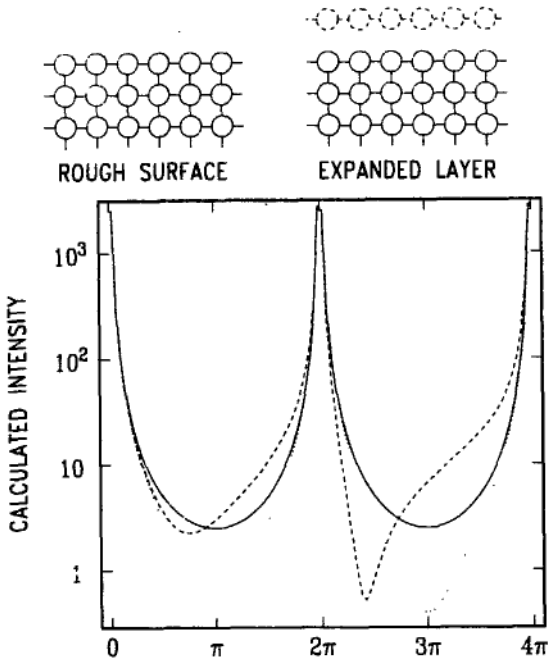

Figure 5. Crystal truncation rod profiles. The full curve shows the CTR for a perfectly sharp surface, as calculated in equation (18). Also shown are the CTRs for a rough surface (dotted curve: equation (23)) and a surface with an expanded top layer (broken curve).

It is instructive to compare the intensity distribution along the rod for the two cases (from equation (17)):

$$I_{2D} = \left| A_0 \frac{e^2}{mc^2} \frac{1}{R_0} F(\boldsymbol{q}) N_1 N_2 \right|^2 \tag{20}$$

$$I_{CTR} = \left| A_0 \frac{e^2}{mc^2} \frac{1}{R_0} F(\boldsymbol{q}) N_1 N_2 \right|^2 \frac{1}{2\sin^2(\boldsymbol{q}\cdot\boldsymbol{a}_3/2)}. \tag{21}$$

Clearly the two kinds of rod have the same order-of-magnitude intensity in the 'valley' far from the Bragg peaks at $\boldsymbol{q}\cdot\boldsymbol{a}_3 = 2\pi l$. The actual intensity observed here in a real experiment is of order of 10 counts per second for a heavy element (such as Pt) using a laboratory-based rotating-anode source, or 10^4 counts per second using a storage ring source in a standard configuration (Moncton and Brown 1983), such as the National Synchrotron Light Source at Brookhaven National Laboratory.

3.2. Surface roughness and CTRs

An alternative way to see the origin of the CTR is to represent the semi-infinite crystal as a *product* of a step function with an infinite lattice. The diffraction pattern is then, by Fourier transformation, the convolution of a reciprocal lattice with the function $(i\boldsymbol{q}\cdot\boldsymbol{a}_3)^{-1}$. It was originally shown by von Laue (1936) and more recently by Andrews and Cowley (1985) that the external surface can thus give rise to streaks emanating from each Bragg peak of the reciprocal lattice. The δ-function Bragg peak becomes

a streak with $|q \cdot a_3|^{-2}$ intensity dependence. Joining adjacent streaks together leads to the $\sin^{-2}(q \cdot a_3/2)$ dependence via

$$\frac{1}{\sin^2(\pi x)} = \frac{1}{\pi^2} \sum_{n=-\infty}^{+\infty} \frac{1}{(x - n\pi)^2}. \tag{22}$$

Also shown in figure 5 are two examples of modified CTRs, corresponding to those of a statistically rough surface (see below) and a surface with a different top layer spacing. The steeper than q^{-2} dependence for the rough surface is simply the consequence of an effective broadening of the step function representing the truncation of the crystal. A simple model of statistical roughness, which was found by Robinson (1986) to work quite well for a variety of samples, is an exponential distribution of heights: layer 0 is assumed to be fully occupied, layer 1 above it (dotted in figure 5) has a fraction β of sites filled, layer 2 has fraction β^2 and so on. This leads to a modification of equation (21) by an additional factor,

$$I_{\text{Rough}} = I_{\text{CTR}} \frac{(1-\beta)^2}{1 + \beta^2 - 2\beta\cos(q \cdot a_3)}. \tag{23}$$

4. Crystal truncation rod analysis

This is the first of five sections that will describe different kinds of measurements that one can make with x-rays to learn about surfaces. Here, for example, we analyse the intensity of the truncation rod to obtain information about the vertical structure. This is useful for examining layered structures with so-called 1×1 reconstructions (see below), in which there is perhaps a lateral or vertical shift of the top plane relative to the bulk, but not a change of the periodicity of that layer. This technique is also very useful in studying interfaces which have different spacings and perhaps different chemical compositions.

CTR analysis is very similar in concept, but not in detail, to the LEED crystallographic analysis (van Hove and Tong 1979). In an x-ray measurement, as we saw in figure 5, the intensity as a function of the perpendicular momentum transfer then passes through the bulk Bragg peaks and has some looping behaviour in between. The looping contains the information about the surface structure of the material, such as the expansion of the layer spacing. This is identical in form to the $I(V)$ spectrum in LEED, except that instead of singular Bragg points where the x-ray intensity goes to a very large value, the electron intensity has attenuated peaks. This is because the penetration of the electrons at 50 eV is very small (≈ 5 Å). We do not use the information near the divergences of x-ray measurements because that tells us only about the bulk; we look instead at the intensity between the bulk Bragg points.

4.1. $NiSi_2$/Si(111) interface

Figure 6 shows a simple interface structure measured by Robinson *et al* (1988a). Nickel has been deposited on top of a Si(111) surface and heated to an appropriate temperature where it reacts to form a good crystalline film of $NiSi_2$. One reason it forms so well is that the lattice parameters of nickel silicide and silicon are within

0.5% of each other at room temperature. Due to this parallel lattice match, the entire structural problem is reduced to one dimension: a determination of the parameter d, the interfacial separation. From that we can figure out the bonding arrangement of the interface. Finer tuning of the technique would allow us to determine the relaxations in the neighbouring silicon or silicide as well. If the interface were ideal, that is, if all of these bonds were ideal silicon–silicon bonds, then the value of d would be $\frac{9}{8}$ of the bulk spacing, a_0 (see figure 6).

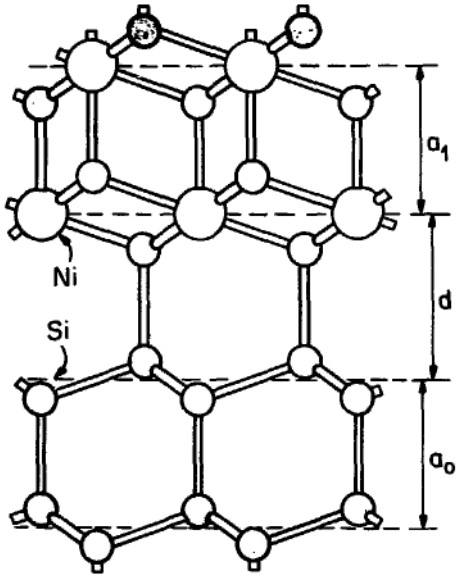

Figure 6. Schematic 'ball and stick' model of a $NiSi_2$/Si(111) interface, defining the structural parameters a_0, a_1 and d.

Let us calculate the diffraction from this system as a function of the single perpendicular component of momentum transfer, q. First of all, we draw the amplitude from the nickel silicide film as a full curve in figure 7(a). This example is a seven-layer film of silicide, so we have a seven-slit interference function $S_7(q \cdot a_3)$ with its broad maximum at the Bragg position in the centre. The substrate gives rise to a truncation rod with its divergence also in the centre (second full curve). However, the $|q|^{-2}$ tails soon overlap with the amplitude from the film. Since the two objects are juxtaposed in the sample, it is their amplitudes that must interfere with each other, not merely their intensities. This is where the structural information about d emerges. On one side of the Bragg peak the intensity goes up, while on the other side the intensity goes down in the superposition (figure 7(b)). The asymmetry is very sensitive to this interfacial parameter d. The best fit to the data is obtained when $d = 1.10a_0$, as can be seen in figure 7(c). This shows a slight *contraction* from the $1.125a_0$ obtained above by considering ideal bond lengths, and agrees well with the results of other techniques (van Loenen *et al* 1985, Vlieg *et al* 1986, Zegenhagen *et al* 1989).

4.2. Other CTR-derived structures

Au(100), Pt(100), and Au(111) all have approximately hexagonal surface layers that are incommensurate with the rest of the crystal. Analysis of the CTRs yields information about the layering of these structures that disregards the details of the

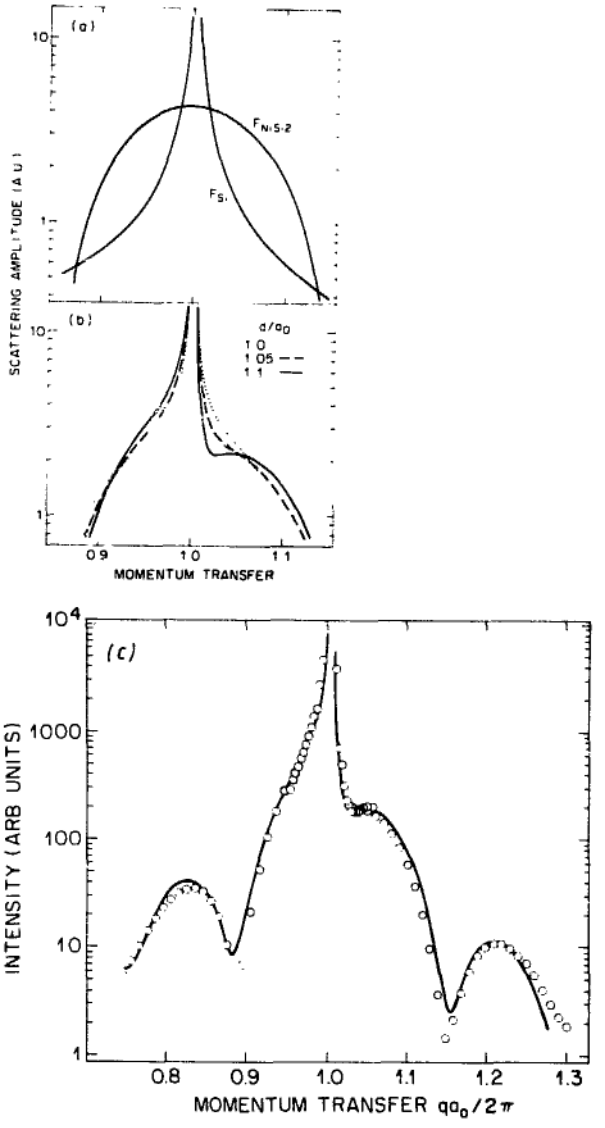

Figure 7. (*a*) Scattering amplitudes in the vicinity of the first-order Bragg peak for the Si(111) substrate and seven-layer $NiSi_2$ film. The momentum transfer is in units of $2\pi/a_0$. (*b*) Total diffraction intensity for various values of d/a_0, found by adding the amplitudes from the substrate and the film with appropriate phase factors and squaring. (*c*) Data (open circles) compared to the best fit (full curve). The best fit gives $d/a_0 = 1.10$. Reproduced from Robinson *et al* (1988a).

incommensurate layer itself (Gibbs *et al* 1988, 1990, Ocko *et al* 1990, Sandy *et al* 1991). These measurements immediately confirmed that the top layer of Au(100) and Pt(100) was 20% denser than the underlying bulk layers, which is seen as a consequence of the hexagonal packing. A later surprise was that Pt(111), a surface not known to reconstruct, also enters this incommensurate state at high temperatures (Sandy *et al* 1992).

Van Silfhout *et al* (1990) studied the structure of the clean Ge(111) surface by means of the CTRs alone, even though it is reconstructed with a c2×8 unit cell. They found a preference for the T4 'adatom' structure (see below). Since only integer orders were used, the structural model could be reduced to a 2×2 unit cell instead of

the full c2×8. Because of this simplification, a large number of structural parameters could be derived that were not determined in the analysis of fractional orders by Feidenhans'l *et al* (1988).

Other structures that have been determined by the analysis of CTR profiles include a number of buried interfaces. The interfaces between amorphous Si and Si(111) and between SiO_2 and Si(111) were examined by Robinson *et al* (1986b). In both cases a good fit to the CTRs was obtained with a model of partially occupied layers on the amorphous side of the interface. Order was lost within a couple of layers. The major difference was that the a-Si/Si(111) interface retained the stacking faults associated with the original 7×7 reconstruction of Si(111). The SiO_2/Si(111) interface has also been studied by Kashiwagura *et al* (1987), Hirosawa *et al* (1990), Iida *et al* (1991), and Cowley and Lucas (1989). GaAs(100)/Si(100) has been measured by Jedrecy *et al* (1990a), Al/GaAs(100) by Marra *et al* (1979), and the GaAs(100)/oxide interface by Kashihara *et al* (1991). The $CaSrF_2$/GaAs(111)B interface, as studied by Hashizume *et al* (1992), showed an absent F layer adjacent to the GaAs.

5. 2D crystallography

This is the oldest of the techniques we will discuss and where the majority of the experimental surface x-ray work around the world has been done. It could be the most generally useful application of x-ray diffraction to surfaces. The object is to figure out the in-plane coordinates of a surface structure by unraveling the positional information encoded in the $F(q)$ of equation (9). We will consider several examples of this in some detail because there are subclassifications of the technique which are specific to the way we solve structures from crystallographic data.

First, we should briefly say what we mean by crystallography in three dimensions. Recall the formula derived earlier expressing the scattering amplitude of a crystal as the sum over all unit cells within the crystal,

$$A_4 = A_0 \frac{e^2}{mc^2}\frac{1}{R_0}F(q)\sum_{n_1=0}^{N_1-1}\sum_{n_2=0}^{N_2-1}\sum_{n_3=0}^{N_3-1}\exp(\mathrm{i}q\cdot(n_1a_1+n_2a_2+n_3a_3))$$

$$= \begin{cases} 0 & q \neq hb_1 + kb_2 + lb_3 \\ A_0\dfrac{e^2}{mc^2}\dfrac{N_1N_2N_3}{R_0}F_{hkl} & q = hb_1 + kb_2 + lb_3. \end{cases} \tag{24}$$

This summarizes the fact that the diffraction pattern from a crystal is a set of δ functions whose weights are the values of the F_{hkl} where

$$F_{hkl} = F(hb_1 + kb_2 + lb_3)$$

$$= \int \rho(r)\exp(\mathrm{i}r\cdot(hb_1 + kb_2 + lb_3))\,\mathrm{d}^3r. \tag{25}$$

The purpose of crystallography in the traditional sense, then, is the determination of the contents of the unit cell, $\rho(r)$, given the intensity of diffraction at a discrete set of points, $q = hb_1 + kb_2 + lb_3$. Equation (25) tells us that F_{hkl} is just the hkl'th Fourier

component of $\rho(\boldsymbol{r})$. This implies that the density is the inverse Fourier transform of the F_{hkl},

$$\rho(\boldsymbol{r}) = \sum_{hkl} F_{hkl} \exp(-\mathrm{i}\boldsymbol{r} \cdot (h\boldsymbol{b}_1 + k\boldsymbol{b}_2 + l\boldsymbol{b}_3)). \tag{26}$$

One might naively think that finding the density is a straightforward application of equation (26). Unfortunately, F_{hkl} is a complex number,

$$F_{hkl} = |F_{hkl}| \mathrm{e}^{\mathrm{i}\alpha_{hkl}} \tag{27}$$

whose amplitude, $|F_{hkl}|$, we measure through the intensity, $I = |A_4|^2$. Consequently the phase factor, α_{hkl}, is the missing quantity. The essence of crystallography, the so-called 'phase problem', is that we measure the amplitude of F_{hkl} but not the phase, and both are necessary to invert the Fourier transform and calculate $\rho(\boldsymbol{r})$.

Now, crystallography has been around a long time and so there are many good tricks for solving this phase problem. We will discuss a couple of them in the next sections but before we do we will first return to the 2D diffraction experiment and think about exactly what it is we measure there. Rewriting equation (25) we have

$$F_{hkl} = \iiint \rho(x, y, z) \exp(\mathrm{i}2\pi(hx + ky + lz)) \, \mathrm{d}x \, \mathrm{d}y \, \mathrm{d}z \tag{28}$$

where we have defined $\boldsymbol{r} = x\boldsymbol{a}_1 + y\boldsymbol{a}_2 + z\boldsymbol{a}_3$ and made use of equations (14), (15) and (16). When we measure in-plane data, we determine the value of F_{hkl} for $l = 0$, which is written F_{hk0} or simply F_{hk}. Then we can rearrange the above equation slightly to obtain

$$F_{hk} = \iint \rho'(x, y) \exp(\mathrm{i}2\pi(hx + ky)) \, \mathrm{d}x \, \mathrm{d}y \tag{29}$$

where

$$\rho'(x, y) = \int \rho(x, y, z) \, \mathrm{d}z. \tag{30}$$

We see that $\rho'(x, y)$ is the projection of the three-dimensional density of the unit cell onto the (x, y) plane, or a 'top view' looking through the structure. Equations (28) to (30) tell us, then, that we can substitute a section of the three-dimensional Fourier transform of the real density with a two-dimensional Fourier transform of the projected density. This result is known as the section-projection theorem, which is very important, incidentally, to the analysis of computed axial tomography (CAT) scans in medicine.

One further point that needs clarification is what is meant by a reconstructed surface. The term reconstruction is defined as a spontaneous change in the periodicity of the crystal at the surface, as illustrated in figure 8. In this example it can be seen that along the horizontal direction of the page the structure has double the periodicity of the bulk. The general nomenclature is an '$n \times m$' reconstruction where n and m

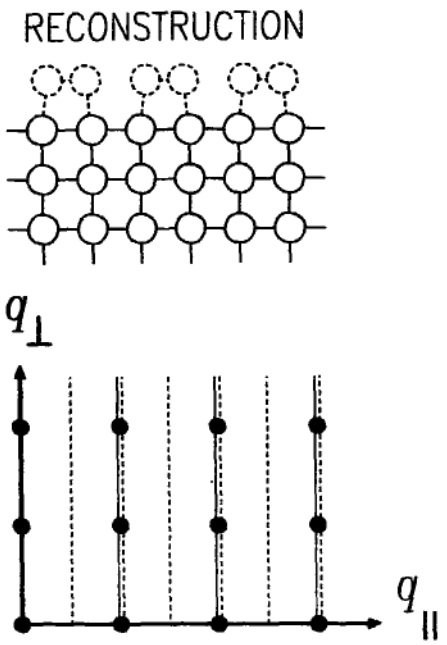

Figure 8. Illustration of diffraction from a 2×1 reconstruction. Full circles represent atoms of a simple cubic crystal viewed from the side. Broken atoms are paired at the surface to double the periodicity. The diffraction pattern below shows bulk Bragg peaks as dots, crystal truncation rods (CTRs) as full lines and contributions from the reconstructed layer as broken lines. At integer-order positions the latter two contributions interfere.

are the multipliers of the unit cell dimensions. Our example is therefore called a 2×1 reconstruction, assuming bulk periodicity out of the plane of the page.

As can be seen in the diffraction pattern of this reconstructed surface in the lower half of figure 8, there are extra lines of diffraction half way between the CTRs of the bulk. We can consider two general regions of reciprocal space of interest to surfaces: the in-plane region ($l = 0$) and the out-of-plane region ($l > 0$). Each of these regions subdivides into 'integer orders', F_{hk}'s with h and k integral, and 'fractional orders' with one or other index fractional. In the case of the in-plane diffraction ($l = 0$) of a crystal with a basis (e.g. FCC or BCC), there will be two kinds of 'integer orders': in-plane bulk peaks where a bulk Bragg reflection occurs, and special points where CTRs intersect the $l = 0$ plane. If we are interested in understanding a surface reconstruction, the fractional-order intensities will be easier to analyse than the integer orders since there is no contribution from the bulk at those positions. Often we start with in-plane, fractional-order data, then extend out-of-plane for 3D information and/or the integer orders to learn about the relation with the bulk crystal. Each of these steps is discussed in detail below.

We have explained the locations of the half-integral spots, but what about their intensities? It is clear that we can get a 2×1 reconstruction in many different ways: by dimers (shown in figure 8), vacancies, or chemical modulation. There can also be more than one layer involved. The exact arrangement within the cell is what determines the relative intensities of the various half-integer spots.

5.1. InSb(111) 2×2 surface

The techniques of 2D crystallography for analysing a reconstructed surface are nicely

illustrated by the InSb(111) and GaSb(111) crystal faces studied respectively by Bohr *et al* (1985) and Feidenhans'l *et al* (1987). When cleaned in ultra high vacuum (UHV) both surfaces show the same 2×2 reconstruction shown in figure 9 (Pedersen 1988). The surface unit cell of InSb(111) without reconstruction (small rhombus in figure 9) contains an indium atom in the top layer and an antimony atom in the layer below. Because InSb is a 'polar' crystal, its $(\bar{1}\bar{1}\bar{1})$ surface instead has the antimony on top and would therefore be expected to have totally different properties; it turns out that it even has a different reconstruction, namely 3×3. In the ideal 2×2 state there are assumed to be four indium and four antimony atoms in each unit cell in a p3m1 planar arrangement; we want to find how they rearrange when the surface reconstructs. To do so, the intensities of the half-integer spots for $l = 0$ were measured and the values of $|F_{hk}|$ derived using equation (20). The results of such an experiment are illustrated in figure 10. This is one sector of the $l = 0$ plane in reciprocal space containing the independent half-integer spots. The rest of the $l = 0$ plane is related by 6mm symmetry (p3m1 plus an inversion centre). The variation in the intensities among the spots is the crystallographic information that tells us where the atoms are in the surface plane. To extract that information we will apply two techniques in succession: the Patterson function and the difference Fourier map.

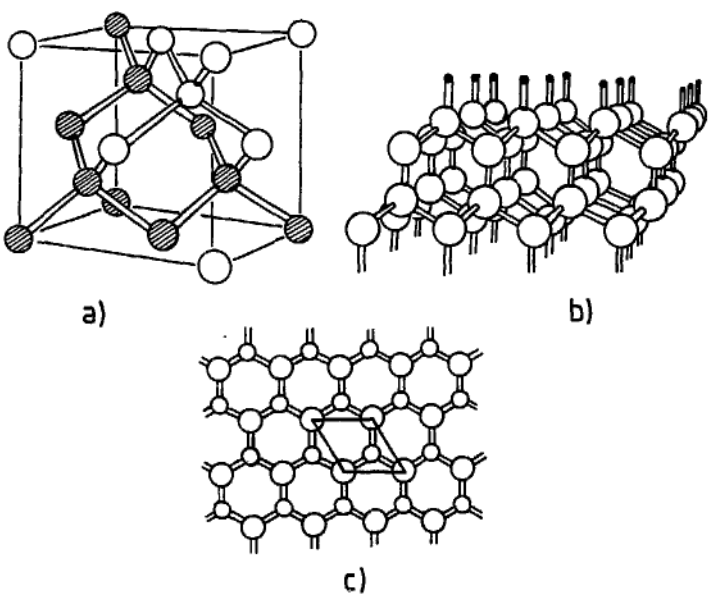

Figure 9. (*a*) Cut through a crystal to form the InSb(111) surface (without reconstruction) in (*b*). (*c*) Top view of the surface with In atoms drawn as large circles and Sb as small circles to show the polar nature of (111). The solid line shows the dimension of the unreconstructed 1×1 surface unit cell. Reproduced from Pedersen (1988).

5.2. Patterson function

We would like to take the Fourier transform of F_{hkl} and thereby obtain $\rho(\boldsymbol{r})$. However, we cannot because the phases are unknown. Instead, we will do the next best thing and take the Fourier transform of $|F_{hkl}|^2$, which is defined to be the Patterson function (Patterson 1934), $P(\boldsymbol{r})$,

$$P(\boldsymbol{r}) = \sum_{hkl} |F_{hkl}|^2 \exp(-i\boldsymbol{q}\cdot\boldsymbol{r}). \tag{31}$$

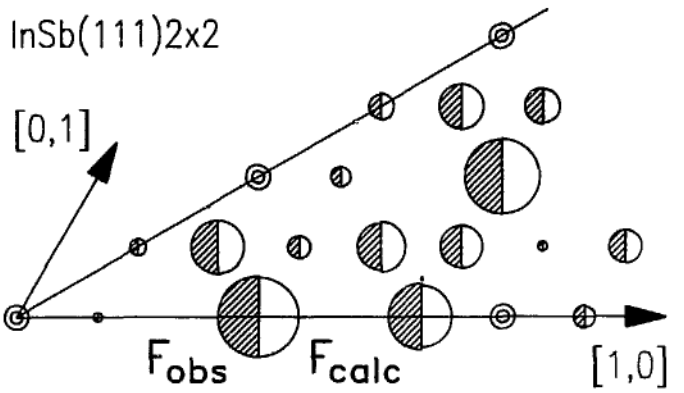

Figure 10. Portion of the $l = 0$ plane in reciprocal space of the 2x2 diffraction pattern for the InSb(111) reconstructed surface. The complete pattern is obtained by the application of the mirror operations of the p6mm plane group. The origin is at the lower left-hand corner and the [10] and [01] vectors denote the h and k axes, respectively. The measured intensities of half-integer order spots are shown as the areas of the shaded, left half-circles, while the values calculated from the final model of Robinson *et al* (1990b) are the open, right half-circles. The double circles are in-plane bulk reflections.

This turns out to be valuable since it is easy to show from equation (25) that

$$P(\boldsymbol{r}) = \int \rho(\boldsymbol{R})\rho(\boldsymbol{r}+\boldsymbol{R})\,\mathrm{d}^3R$$
$$= \langle \rho(\boldsymbol{r})\rho(0)\rangle \tag{32}$$

where $\langle \rho(\boldsymbol{r})\rho(0)\rangle$ is called the electron density–density autocorrelation function for the unit cell. The utility of this function is illustrated in figure 11. Here the electron density of a 1D structure consisting of three atoms with Z_1, Z_2 and Z_3 electrons, respectively, is shown in figure 11(a) and the corresponding Patterson function in figure 11(b). A graphical way to generate $P(r)$, the correlation function of $\rho(r)$ with itself, is to shift a copy of the density pattern of part (a) a distance r and overlay it on the unshifted $\rho(r)$. Then the shifted and unshifted patterns are multiplied together and the area under the resulting curve is calculated, giving $P(r)$. After a little consideration it is apparent that all of the interatomic distances in $\rho(r)$ will appear in $P(r)$. Both distances and directions of the vectors will be preserved. Furthermore, the strength of the Patterson peaks will be proportional to the product of the electron densities of the two or more atoms which produced that peak. Consequently, the largest peak will be at the origin and $P(r)$ will be symmetric about the origin.

We wish to produce a 2D Patterson function. From equation (25) and the fact that $\rho(\boldsymbol{r})$ is real it follows that $|F_{hk}| = |F_{-h-k}|$. Equation (31) then reduces to

$$P(x,y) = 2\sum_{hk} |F_{hk}|^2 \cos\left[2\pi(hx+ky)\right] \tag{33}$$

which is also a real quantity. Figure 12(a) is a contour map showing the Patterson function for InSb(111) obtained by Bohr *et al* (1985) from the intensities in figure 10. There are four clear non-origin peaks that must correspond to interatomic vectors in the surface structure. The bulk structure projected into the (111) plane is a

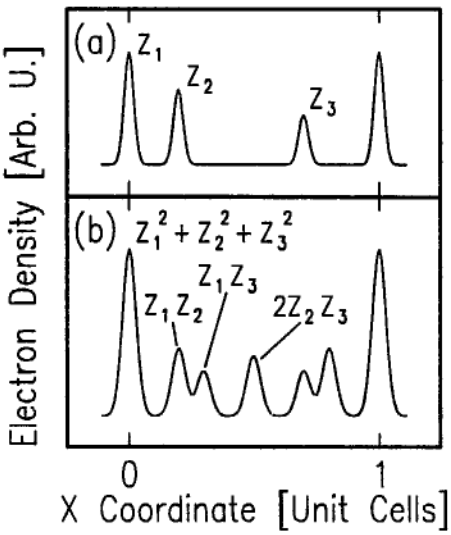

Figure 11. The Patterson function of a one-dimensional unit cell. (*a*) The electron density of a 1D structure consisting of three atoms with Z_1, Z_2 and Z_3 electrons, respectively. (*b*) The corresponding Patterson function for this structure. Adapted from Warren (1969).

honeycomb arrangement of atoms, in which the repeating unit is a covalently bonded hexagon, shown as open circles in figure 12(*b*). If the hexagon is placed in a 2×2 unit cell, interatomic vectors are the open circles shown in figure 12(*c*). If the hexagon is distorted roughly to conserve bond length, as the closed circles in figure 12(*b*) indicate, the peaks in the Patterson function move to the positions indicated in figure 12(*c*), which are exactly those observed in figure 12(*a*).

Thus we have explained the location of the peaks in the Patterson function by this distorted hexagon. Of course, we do not know yet which atoms are indium and which are antimony, but at least we know that this is a basic structural element of the surface. To check our answer we take the hexagon, put it into the 2 × 2 unit cell, and calculate what the observed intensities should be. To do so, we refer back to the definition of F_{hkl} in equation (7), as the sum of the atomic form factors of each atom in the unit cell. Up until now we have found it best to think of F_{hkl} as the Fourier transform of the unit cell density, equation (9), but for the present calculation equation (7) provides the more convenient definition. We therefore arrive at

$$|F^c_{hk}|e^{i\alpha^c_{hk}} = \sum_{j=1}^{6} f_j(q_{hk}) \exp(i2\pi(hx_j + ky_j)) \tag{34}$$

where the six atoms in the 2 × 2 unit cell are at coordinates (x_j, y_j) and have form factors $f_j(q_{hk})$. From this the predicted intensities of the various spots can be derived. However, the results are found not to agree very well with the observed values. This may be discouraging, but the Patterson function analysis gives us confidence that our distorted hexagon is at least a major part of the structure. Clearly, we need a method to tell us what we have missed. The next technique does exactly that.

5.3. Difference Fourier map

We begin by using equation (26) to write down the unit cell density for the true

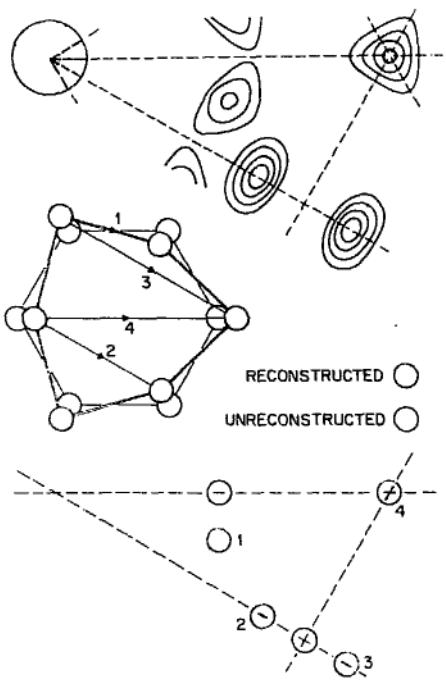

Figure 12. (*a*) Repeating unit of the Patterson function calculated from the intensities shown in figure 10. Positive contour levels above zero are shown. Broken mirror lines surround the asymmetric repeating unit. The shaded circle is the origin peak. (*b*) Distortion of a hexagonal arrangement of atoms taken from the projected unreconstructed InSb(111) surface. (*c*) Pair-correlation peaks 1 to 4 derived from vectors 1 to 4 in (b). Reproduced from Bohr *et al* (1985).

structure, $\rho^{o}(x,y)$, and the initial model structure, $\rho^{c}(x,y)$,

$$\rho^{o}(x,y) = \sum_{hk} |F^{o}_{hk}| e^{i\alpha^{o}_{hk}} \exp(-i2\pi(hx+ky)) \tag{35}$$

$$\rho^{c}(x,y) = \sum_{hk} |F^{c}_{hk}| e^{i\alpha^{c}_{hk}} \exp(-i2\pi(hx+ky)). \tag{36}$$

Here the superscript 'o' refers to the observed values while 'c' refers to the values calculated from the distorted hexagon in equation (34). Note that we do not yet know α^{o}_{hk}; it is the set of missing phases.

Next we need to assume that, even though the model density is not completely correct, it is close to the true density. In particular we assume that our model is only wrong in a few places; that it has the proper location of most of the atoms but is just missing one or two. Since the phases come from the structure as a whole, it follows that the unknown, true phase is close to the phase calculated from the model,

$$\alpha^{o}_{hk} \approx \alpha^{c}_{hk}. \tag{37}$$

With this approximation we can now calculate the difference between the two electron densities, which will be a map of the positions of all the mistakes we have made in the structure,

$$\rho^{o}(x,y) - \rho^{c}(x,y) = \sum_{hk} (|F^{o}_{hk}| - |F^{c}_{hk}|) e^{i\alpha^{c}_{hk}} \exp(-i2\pi(hx+ky)). \tag{38}$$

Figure 13 is the resulting difference Fourier map. Centred on one of the three-fold axes and accented for clarity is the distorted hexagon we obtained from the Patterson function. Upon examining this map we discover that the only place where there is a significant peak is at the other three-fold axis. Thus, we can see from this difference calculation that we need one more atom in the structure and that it should sit at this three-fold position. When we put that seventh atom in the unit cell we get extremely good agreement between the observed and calculated structure factors. We can then conclude that we have arrived at the correct structure.

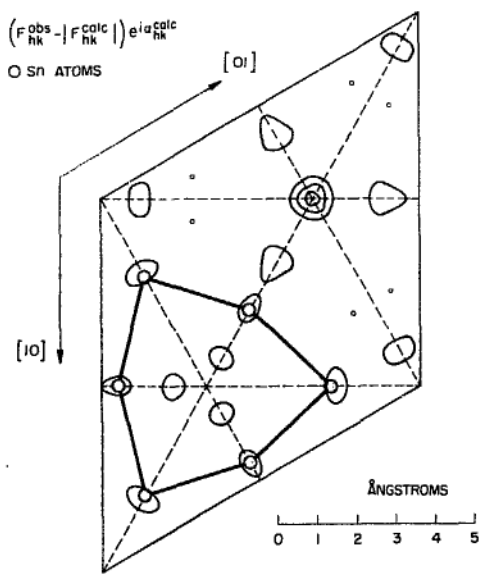

Figure 13. Difference Fourier map of one InSb(111) unit cell. Positive contours above zero are shown. The distorted hexagon of figure 12(*b*) is drawn with thick full lines.

Figure 14(*a*) shows the final picture, true for both InSb(111) and GaSb(111) (Feidenhans'l *et al* 1987). The top panel is an overall view of the surface with an enlarged view of one 2×2 unit cell in the centre. Starting with the eight atoms of the unreconstructed unit cell we find that there are only seven atoms left, meaning the one in the corner is missing, producing a vacancy site. The antimony closest to the vacancy moves towards it, distorting the hexagonal bonding of the bulk stucture viewed along (111). Meanwhile, the seventh atom is able to stay where it was. At the bottom of figure 14(*b*) are listed some of the bond lengths and angles for InSb(111) and GaSb(111) as well as GaAs(111) (Tong *et al* 1984), which has a similar structure. The surface bond lengths, seen here as their 2D projections, are found to be very close to the bulk values in all three cases. This is a strong argument suggesting the surface is flat. Consequently the projected bond angles which we observe are close to the actual bond angles. The trend in bond angle from As to Sb reflects the increasing tendency down the group V elements to form p-type bonds (90° angle) instead of sp^3 (109° angle). All atoms in the bulk have the 109° sp^3 configuration. Similarly, the group III element (indium or gallium) has bond angles around 120°, typical of sp^2 bonding, which it prefers in small molecules (Wells 1985). Thus we find that both the group III and group V elements in the surface revert to molecular configurations rather than the fully ionic sp^3 state they achieve in the bulk.

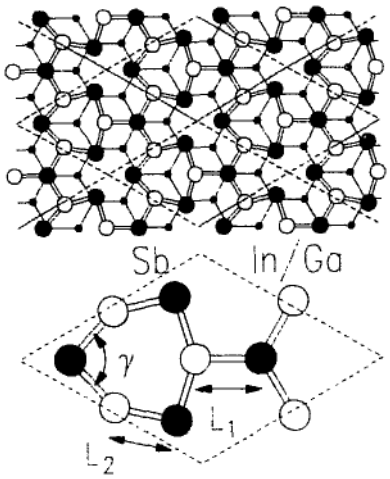

	InSb	GaSb	GaAs
L_1	2.87(5)	2.66(6)	2.41
L_2	2.82(5)	2.64(4)	2.42
Bulk	2.81	2.64	2.45
γ	96°	98°	104°

Figure 14. (*a*) Overview of a large region of the III–V(111) surface with its 2×2 reconstruction. (*b*) Enlarged view of the reconstructed unit cell defining projected bond lengths and angles. (*c*) Values of the structural parameters for various III–V(111) surfaces. InSb(111) is from Bohr *et al* (1985), GaSb(111) from Feidenhans'l *et al* (1987) and GaAs(111) from Tong *et al* (1984).

5.4. Interference at truncation rod positions

We now turn to the next level of detail in this structure, which allows us to discuss another technique of 2D crystallography, the use of the crystal truncation rod information. Up to now we have considered the structure to be an 'isolated monolayer' in the sense of figure 3. Rather than just looking at the fractional-order intensity we are now going to consider the intensity at the integral-order positions, where we have contributions both from the known bulk structure and from the surface structure we have just derived. The reason we would want to do such a thing is that we do not know the 'registry', or how the surface layer sits on top of the bulk. It turns out there are six possible registries, as drawn in figure 15. Firstly, there are two possible rotational orientations for the surface layer. The bulk layers of an FCC crystal viewed along (111) alternate in an triple sequence, usually denoted ABCABC.... This raises the question of which is the last bulk layer beneath the surface: A, B or C? Stated another way, we have to choose which of the three three-fold axes in the p3m1 surface unit cell lines up with the corner of the bulk unit cell.

Under each candidate in figure 15 is written the χ^2 value. This is a measure of agreement of the intensities of four integer-order spots, where

$$\chi^2 = \frac{1}{N-P}\sum \frac{(|F_{hk}^{c}| - |F_{hk}^{o}|)^2}{\sigma_F^2} \tag{39}$$

where N is the number of measurements (four here), P is the number of free fit parameters (0 here) and σ_F is the measured uncertainty in the value of $|F_{hk}^{o}|$. This

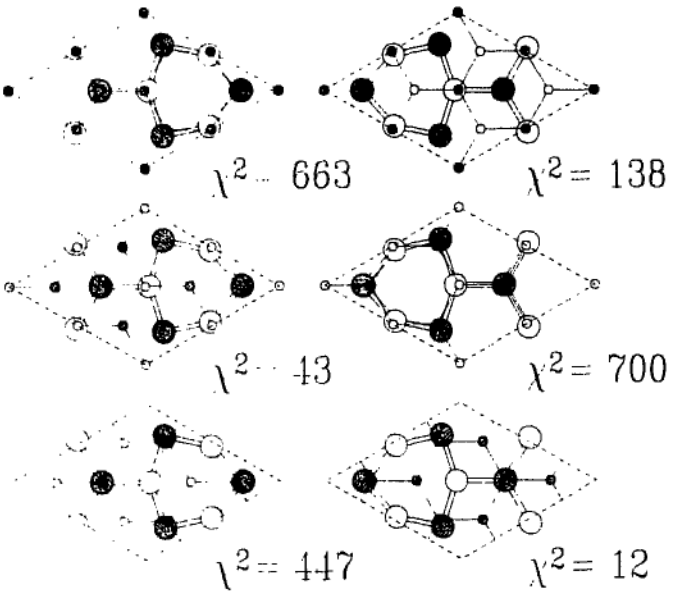

Figure 15. Possible registries of the GaSb(111) 2×2 reconstruction with the bulk. Values of χ^2 given by equation (39) for the agreement of the integer-order intensities with the measured values clearly identify the bottom right combination as the correct one.

function is widely used as a goodness-of-fit criterion in the optimization of a model with data (Bevington 1969) to correctly account for the measured errors. In figure 15 the arrangement in the lower right of the figure has the smallest χ^2 by far and so is the correct choice. We notice that it makes the fewest possible changes from the bulk structure, a reassuring result. Some of the wrong candidates are unrealistic in that bonds could not be connected. The correct answer has neither a stacking fault nor a reverse top layer, and it has the same order in the stacking sequence that we would expect from ordinary ABC stacking.

5.5. Further improvements on the InSb(111) structure

The final structure detailed in figure 14 was refined in two dimensions by least-squares minimization of a χ^2 given by equation (39) to obtain the final parameters listed. Debye–Waller temperature factors were included at that time and found to be slighly enlarged from the values from bulk InSb and GaSb (Bohr *et al* 1985, Feidenhans'l *et al* 1987). Nevertheless, the final χ^2 values were 3.8 and 4.2, respectively. Now χ^2 is a measure of the total error in standard deviation units, and the σ_F values input were derived carefully from the reproducibility of the data and so believed to be representative. The value of χ^2 greater than unity informs us that something is still missing from the structure.

Belzner *et al* (1989) considered this point and suggested some possibilities. They found that anisotropic temperature factors were not sufficient and concluded by means of difference maps as used above that extra density was needed in the vacant site at the corner of the 2×2 unit cell. They proposed that the vacancy was partially filled by a disordered In present in a fraction of the unit cells. In this way they obtained χ^2 close to 1.0.

Robinson *et al* (1989a) reconsidered the data also to explain the discrepancy in

χ^2. Their model was of small second-layer displacements that slightly perturb the structure factor. This gave χ^2 values of 1.5 and 1.4 for InSb(111) and GaSb(111) which are close to unity too. The final calculated structure factors are compared with the data in figure 10. It is important to note, however, that on the grounds of χ^2 alone it is impossible to distinguish between this model and the one of Belzner *et al* (1989), although second-layer displacements makes a less exotic explanation. The measurements needed to make the distinction between the disordered one-layer and the two-layer models are out-of-plane diffraction intensities, which are the subject of the next section. No more than a tiny range of perpendicular momentum transfer was available at the time of the original study because of instrumentation limitations.

5.6. Results obtained by 2D crystallography

Reconstruction is relatively rare among elemental metals. Adsorbates on metals, on the other hand, are frequently seen to order into superstructures that can be analysed in just the same way as reconstructed surfaces, and there are many cases of these known. Historically it was once assumed in the absence of structural data that adsorbates simply attach to metals without modifying the substrate. The commonly used language of 'hollow sites', 'bridge sites' and 'atop sites' on surfaces reflects this assumption. As more and more systems were examined in detail, substrate adaption was found to be present as well. This can be dramatic when the density of surface atoms changes to form vacancies or added clusters.

This is clearly seen on Cu(110) and Cu(100) surfaces that both reconstruct in the presence of oxygen to form 'missing row' structures. In-plane x-ray studies were done by Liang *et al* (1985) and Feidenhans'l *et al* (1990a) for Cu(110) and by Robinson *et al* (1990b) for Cu(100), respectively. The two structures are closely related in having the same basic structural element: a chain of Cu–O–Cu–O–Cu structure along one of the in-plane crystallographic [100] directions. Adjacent to the chains there is an entire atomic row missing. Coulman *et al* (1990) showed with scanning tunnelling microscopy (STM) that the chains assemble on existing clean terraces of (110) and so they suggested the term 'added row' would be more appropriate, although the final fully ordered 2×1 state is identical. At higher coverages, oxygen gives rise to a c6×2 structure on Cu(110). Feidenhans'l *et al* (1990b) analysed this structure as well to find that the extra oxygen is accommodated in a closer packing of Cu–O–Cu–O–Cu chains, two per three substrate unit-cells, and also in O–Cu–O bridging arrangements. This structure is shown in figure 16.

Semiconductors are covalent crystals for which the topological properties of the chemical bonds tend to lead to a rich variety of reconstructions. Most notable are the clean Ge(111)c2×8 and Si(111)7×7 structures studied with in-plane x-ray diffraction by Feidenhans'l *et al* (1988) and Robinson *et al* (1986a, 1988b), respectively. The Si(111)7×7 structure has been a major milestone in the history of surface science, and is itself the subject of a recent review by Haneman (1987). Both the Si and Ge structures are based on a local configuration called a T4 'adatom' that is constructed by adding a Si or Ge tetrahedron face down over three otherwise dangling bonds emerging from an ideal (111) surface. As we will see further below this is a widespread element of almost all semiconductor (111) surfaces. It has an interesting distribution of strain that was shown by Northrup (1986) and later by Vanderbilt (1987) to be energetically favourable mainly because of the reduction of dangling bonds. The pivotal role of strain in the story of the stability of the 7×7 has been revealed by the analysis of the crystallographically derived coordinates of the atoms by Pedersen *et*

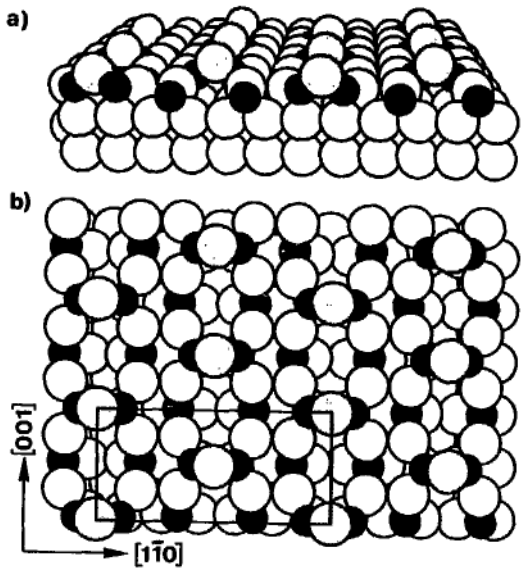

Figure 16. (*a*) Oblique and (*b*) plan views of the Cu(110)/O c6×2 structure determined by Feidenhans'l *et al* (1990b). Black atoms are oxygen and the white ones are copper, with the top-layer bridging sites shaded for clarity.

al (1988) and by Robinson (1988b). There are two independent T4 adatoms in the unit cell, both of which demonstrate the same pattern of inward lateral displacements of the near neighbours. Ge(111) also forms both a 7×7 and a closely related 5×5 structure in the presence of Sn (Pedersen 1988). Here Sn, which lies immediately below Ge in the periodic table, acts to form a surface alloy since its occupation at the various sites in the structure appears to change with coverage. The order of phases for increasing Sn coverage on Ge(111) is $\sqrt{3} \times \sqrt{3}$, 7×7 then 5×5 (Ichikawa and Ino 1981). GeSi alloys obtained by Gossmann *et al* (1984) by deposition of Ge on Si(111) also show the 5×5 reconstruction. Even pure Ge(111) was found by Gossmann *et al* (1985) to switch to the 7×7 structure when a moderate (1–2%) compressive strain is applied by suitable epitaxy on Si(111).

Meanwhile, the 7×7 was shown by Takayanagi *et al* (1985) to contain, in addition to the adatoms, an elegant network of triangular stacking faults and bordering dimers that have p6mm symmetry, while the ideal bulk has only p3m1 surface symmetry. This increased symmetry was confirmed experimentally by Robinson (1987) and is an interesting exception to Jona *et al* 's (1982) rule of surface structures with lower symmetry that give rise to corresponding twin domains.

Si(100) and Ge(100) have 2×1 reconstructions that were first studied by Jedrecy *et al* (1990b) and by Eisenberger and Marra (1981) using in-plane x-ray diffraction. Both structures are simple dimers in which surface atoms pair together to share one of the two covalent bonds that would be dangling into the vacuum. The difference between them is that, at least at room temperature, Si(100) has an asymmetric dimer with its centre of mass shifted to one side, with the effect of buckling the dimer by tilting it. That Ge(100) has a symmetric dimer has since been confirmed by Grey *et al* (1988) in a more comprehensive out-of-plane study (see below).

The GaAs(100) surface has a number of stable ordered configurations that depend on the surface stoichiometry, and hence on the preparation conditions. One readily

achieved state lies fully at the As end of the stoichiometry spectrum, under As saturation conditions. This is the c4×4 structure studied by Sauvage-Simkin *et al* (1989). Surprisingly it is not a pure structure but composed instead of a mixture of two structures: one has two parallel As–As dimers per unit cell (similar to those in Ge(100)) and an effective As coverage of 0.5, while the other has three dimers and a coverage of 0.75. It seems probable that the ratio that forms depends on the exact pressure of As_4 during growth, but this was not investigated. As/Si(100) also has a dimer structure in a 2×1 unit cell, but unlike the clean Si(100) surface, the dimer is symmetric (Jedrecy *et al* 1990b). Conversely, the hydrogen stabilized GaAs(100) surface exposes Ga as the top layer and forms a 4×1 structure containing asymmetric Ga dimers (Kisker *et al* 1990).

Deposited metals on semiconductors can often produce incommensurate structures with peaks at irrational positions or high-order commensurate structures. The examples here are Pb/Si(111) studied by Grey *et al* (1989) and Au/Si(111) studied by Feidenhans'l *et al* (1989), respectively. These are close-packed structures involving noble or less reactive metals where the commensurability is determined by the relative lattice parameters of the metal and semiconductor. These systems may show interesting commensurate/incommensurate phase transitions, analogous to the well-studied noble gas/graphite systems (Horn *et al* 1978, McTague *et al* 1982, D'Amico *et al* 1984).

Similarly, a number of studies have been made of metal-on-metal structures. Crystallographic analysis has been used to identify the phases concerned. Heavy metals such as Pb on Cu(110) and Cu(100) have shown an interesting series of structures, both commensurate and incommensurate (Marra *et al* 1982, Brennan *et al* 1986, Lee *et al* 1990).

Structural determinations have also been carried out for a variety of buried interfaces by measurement of in-plane superstructure reflections: SiO_2/Si(100) by Renaud *et al* (1991) and by Ourmazd *et al* (1989), and buried reconstruction of GeSi(111) 5×5 under *a*-Si by Mizuki *et al* (1988), the GaAs(100)/Al interface by Akimoto *et al* (1987), and ZnSe(100) under growth by chemical vapour deposition (CVD) by Fuoss *et al* (1989a). Fuoss *et al* (1989b) showed that the structure of this CVD grown ZnSe(100) face contains symmetric Se–Se dimers.

6. 3D structure analysis

The next development is to include the 3D information of the rod profile. This simultaneously incorporates the two previously discussed techniques, CTR analysis and 2D crystallography, and allows us to analyse multilayer reconstructions at a surface or at an interface between two different materials. Historically this generalization of the technique has been a recent development in the field for instrumental rather than conceptual reasons.

Figure 17 is a sketch of the general form of the 3D data. Recall that in 3D crystallography the structure factors would be written F_{hki}. We now write $F_{hk}(l)$ to emphasize the continuous nature of diffraction of 2D objects. To be even more clear, we will use the explictly continuous variable q_z, the component of momentum transfer normal to the layers, in place of l. Both notations are used in practice and differ only in the units: q_z is in $Å^{-1}$, while l is in units of $|b_3|$ according to equation (16). Figure 17(*a*) shows the variation in the intensity, which is proportional to $|F_{hk}(q_z)|^2$,

as a function of q_z for a single layer structure. For 2D crystallography we have been focusing all our attention on $q_z = 0$. Recall from the discussion of figure 4(a) that the diffraction intensity along a rod from a 2D structure (e.g. a monolayer of atoms) is independent of q_z. The only modification that has been made in figure 17(a) is the inclusion of a form factor and possible Debye–Waller temperature factor that causes the curve to drop slightly with total $|q|$. Figure 17(b) shows the situation for a multilayer structure where we see the appearance of wiggles in the diffraction. As explained in figure 2 and the section on CTR analysis, an N-layer film will produce a characteristic N-slit diffraction pattern with $N - 2$ subsidiary peaks between the primary maxima, just as in optics. A multilayer reconstruction will produce the same pattern and so the depth of the reconstruction can be found by just taking the period of the oscillation in Å^{-1} and dividing it into 2π.

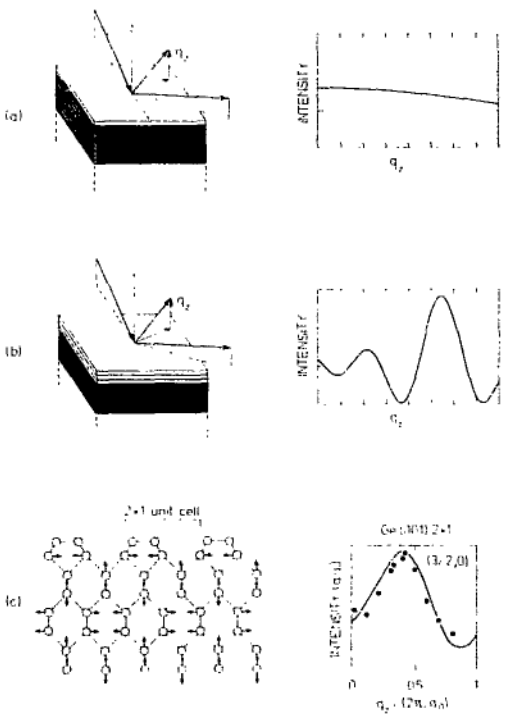

Figure 17. Illustration of diffraction along a fractional order rod. (a) Simulated diffraction from a single reconstructed layer. (b) Simulated diffraction from several reconstructed layers. (c) Measured diffraction (dots) from the Ge(100) 2×1 surface compared with a model in which the first eight layers participate in the reconstruction (full curve). Reproduced from Grey and Feidenhans'l (1988).

6.1. Ge(100) surface

Figure 17(c) shows real data for the Ge(100) surface (Grey and Feidenhans'l 1988). This has the 2×1 dimer reconstruction we encountered above. This is similar to that of figure 8, except that Ge is a crystal of the diamond structure instead of simple cubic. A large set of half-order rods were measured (Grey *et al* 1988) by moving the detector out of the plane of the surface. This represented the state of the art at that time.

The rapid oscillation of the data with q_z calls for a model with reconstruction going deep into the crystal. For the dimer structure shown in figure 17(*c*), this implies a strain field originating from the displacements in the surface associated with the formation of the dimer. The number of layers can be estimated directly from the period of oscillation in q_z, which is 1 reciprocal lattice unit ($2\pi/a_0$) here. This implies approximately one direct space unit cell spacing (a_0), which is the required depth of reconstruction. There are four layers in a unit cell in Ge. To get a good fit, Grey *et al* (1989) made a model with significant displacements eight layers into the bulk, as shown. Since the deeper displacements are very small, the effective average depth is consistent with the four layers. The model gives the full curve through the data in figure 17(*c*).

6.2. W(100) surface

Another good example is the measurement of the reconstructed W(100) surface (Altman *et al* 1988) in figure 18. The measurements shown were obtained with a four-circle diffractometer by tilting the sample to gain perpendicular momentum transfer. The necessary diffractometer setting calculations to control the incidence and exit angles for such an instrument were derived both by Mochrie (1988) and by Robinson (1989). A fairly severe resolution correction to the intensity was also required to account for misalignment of the rod with the resolution direction in this geometry (Robinson 1988a).

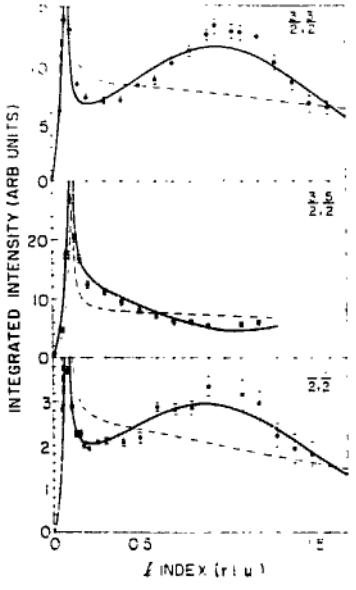

Figure 18. Half-order diffraction rods for the W(100) $\sqrt{2} \times \sqrt{2}$ R45° surface. Measured intensity (points) is compared with a model (full curve) in which the top two layers reconstruct. The broken curve corresponds to a one-layer model. The perpendicular momentum transfer l is the same as q_z after conversion into units of $2\pi/a_0$. Reproduced from Altman *et al* (1988).

Again, sinusoidal oscillations in the intensity as a function of q_z are apparent. This time the period is closer to 2 reciprocal lattice units, implying a direct space distance of half a unit cell or one layer spacing. In fact the layer spacing is determined

in the fitting of the data (solid curve, see below) to be 1.52 Å, slightly relaxed from the bulk spacing of 1.58 Å.

At small q_z each curve shows a fairly narrow feature that we have not encountered before. The intensity rises from zero at $q_z = 0$ through a peak and then drops back to the level of the rod structure factor. This is a dynamical effect due to refraction from the surface. The enhancement of intensity occurs when either the incident or exit rays (or both) come close to the critical angle for total external reflection. It will be dealt with fully in the next main section on evanescent wave techniques.

Tungsten has the BCC structure in the bulk. This means the ideal W(100) surface is not close-packed and has the relatively low coordination of 4 for the surface atoms. Debe and King (1977) showed that it reconstructs by lateral displacements of the top layer into chains, as shown in figure 19. The chains add two extra bonds per surface atom bringing the coordination up to six. The resulting $\sqrt{2} \times \sqrt{2}$ R45° unit cell is indicated with broken lines. The observation of oscillation along the rods implies immediately that the structure is more complicated still: a single reconstructed layer would give the broken intensity curves with no oscillation in figure 18. Altman *et al* (1988) showed that in addition to the zig-zag pattern of displacements in the top layer, a layer of similar but smaller displacements was needed below. Figure 19 shows the final structure. The top layer displacement is 0.24 Å and the second layer 0.046 Å.

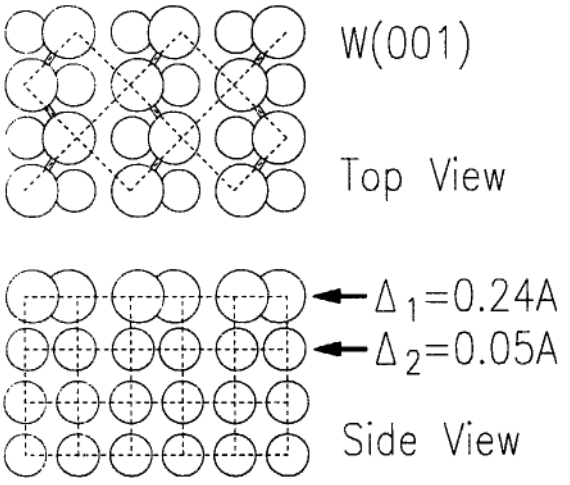

Figure 19. W(100) $\sqrt{2} \times \sqrt{2}$ R45° structure showing top and side views of the atomic positions in the surface. Displacements in the first and second layers from ideal BCC bulk sites are denoted Δ_1 and Δ_2. Prior to the x-ray work only the top-layer displacements were known to exist.

Steady improvements in instrumentation have further increased the accessible range of perpendicular momentum transfer, either by moving the detector out of the plane of the surface or more recently by use of a fifth diffractometer α axis that effectively rotates the incident beam direction (Vlieg *et al* 1987). Nowadays perpendicular momentum transfers of 5 $Å^{-1}$ are routinely available, with corresponding improvements in accuracy of structures in the perpendicular direction.

6.3. Results obtained by 3D structure analysis

A simple example of a 3D structural determination is of the Cu(100)/S p2×2 adsorbate structure studied by Vlieg *et al* (1990b). Because the single S atom sitting in a four-

fold hollow site induces a reconstruction in the substrate, there is beating of the intensity along the half-order rods. The period of beating establishes the spacing (1.19 Å). The amplitude of modulation determines the sign and magnitude of the substrate displacements (0.03 Å away from the S).

We previously met the T4 adatom structure on clean semiconductor (111) surfaces. Here the adatom lies directly above a third layer atom but is not bonded directly to it, except by a so-called 'backbond'. Both atoms have radial bonds to three second layer atoms that are drawn inwards. The closest packing of such units is in a $\sqrt{3} \times \sqrt{3}$ unit cell. In such a state, T4 was predicted by Northrup (1984) to be considerably more stable than the apparently more openly bonded H3 site. The $\sqrt{3} \times \sqrt{3}$ T4 is also an ideal arrangement for an adsorbate on a semiconductor (111) surface, and represents the structure of Sn/Si(111) studied by Conway *et al* (1989), Pb/Ge(111) studied by Feidenhans'l *et al* (1986) and Pedersen *et al* (1987), Bi/Si(111) studied by Takahashi *et al* (1985, 1987a, b) and Sn/Ge(111) studied by Pedersen *et al* (1987). In each case, the induced strain leads to inward contraction of the immediate Si neighbours of the adatom. This results in perpendicular displacements in layers 3 and 4 and consequently to outward relaxation of the three fourth nearest neighbours in the fifth layer. The pattern of inward motion in layer 2 and outward motion in layer 5 is faithfully reproduced in all the above-mentioned examples.

The B/Si(111) $\sqrt{3} \times \sqrt{3}$ structure is the first exception to this pattern. Here the fifth layer displacement is in the opposite sense and considerably smaller. Headrick *et al* (1989b) explained the anomaly by showing that the B atom occupies an altogether different site, the substitutional S5 site. The B–Si bondlength is around 15% shorter than Si–Si, whereas each of the metals forms a longer bond, so the S5 site is accommodated with less resulting strain than the T4 site. It consequently results in very different behaviour of this surface towards overgrowth of Si and explains why a single layer of B can be largely retained at a Si/Si crystalline interface, while this situation is untenable with Ga for example (Headrick *et al* 1989a, 1990).

The Ag/Si(111) $\sqrt{3} \times \sqrt{3}$ structure is the second exception. This is one of the most widely studied surfaces of all because of its apparently simple structure coupled with its technological importance in semiconductor contacts. The first controversial issue is the Ag coverage itself: the majority of evidence favours one monolayer (ML), implying three Ag atoms per $\sqrt{3} \times \sqrt{3}$ unit cell. This coverage already implies it cannot be the simple T4 structure. Wilson and Chiang (1987) published STM images showing a hexagonal mesh of protrusions resembling a honeycomb. The problem here is that there are only two protrusions per unit cell, inconsistent with the coverage of one ML. They concluded instead that the coverage was $\frac{2}{3}$.

Then came two independent 3D x-ray diffraction studies of Ag/Si(111) $\sqrt{3} \times \sqrt{3}$. One was by Takahashi *et al* (1988) using the novel approach of energy dispersive diffraction at a fixed 133° scattering angle. They used thin samples to reduce background. Their data included nine integer orders and seven fractional orders but were limited to rather large values of perpendicular momentum transfer. They concluded that the Ag atoms do indeed have one ML coverage, and form a 'trimer', in the sense that they are displaced away from ideal high symmetry sites in a three-fold symmetric manner to form a monolayer structure with a variety of interatomic spacings. The pattern was apparently inconsistent with Wilson and Chiang (1987), however. The Si layer immediately below was unmodified and found to be a distance of 2.9 Å away.

The second x-ray diffraction study was by Vlieg *et al* (1989a) using 3D data of fractional-order rods only. They found a ML Ag structure similar to Takahashi *et al*'s,

but with an extra top layer of Si containing two atoms per unit cell which gave rise to the honeycomb pattern seen in the STM. Refinement of a large in-plane dataset revealed that reconstructions were present also in the underlying Si layers.

Ding *et al* (1991) performed a total energy calculation on this same system and found consistency with Takahashi *et al*'s (1988) Ag trimer model. They did *not* need to include the Si honeycomb of Vlieg *et al* (1989a), but otherwise agreed with the atomic positions they found for the remaining layers. The calculation clearly ruled out models containing Ag honeycombs, as suggested by Wilson and Chiang (1987) using STM. However, they were able to explain the honeycomb appearance of the STM images as unoccupied electronic states on the Ag trimer layer. The peaks in the STM image align with the centres of the trimers, not where the atoms themselves are.

The surfaces of Au(110) and Pt(110) have a simple 'missing row' reconstruction in which alternate rows of atoms are present and absent. This was first studied with LEED by Moritz and Wolf (1979). The structure exposes (111) facets on the surface, which, due to relaxation of the coordinates, leads to a greater effective coordination of these atoms, and hence higher stability. The first application of x-ray diffraction to Au(110) was by Robinson (1983). That experiment proved the missing row structure and led to the discovery of large subsurface relaxations. Later Vlieg *et al* (1990a) measured extensive 3D data for both Au(110) and Pt(110) and found further subsurface relaxations, including significant contributions from the fourth layer. The presence of relaxations was confirmed with LEED by Moritz and Wolf (1985) who discovered in addition a third-layer buckling. The result is one of the most accurately known surface structures of all and serves as an interesting benchmark of precision in structure determination. Typical errors for x-ray surface crystallography are 0.01 Å parallel to the surface and 0.1 Å perpendicular to it (Vlieg *et al* 1990a), while for LEED crystallography they are more like 0.1 Å parallel to the surface and 0.01 Å perpendicular (Fery *et al* 1988). The complementarity of the two techniques arises from the different ranges of total momentum transfer typically used.

7. Evanescent wave method

Here we discuss the meaning of the features we saw in figure 18 at small q_z values where the surface diffraction intensity was observed to rise. All of the methods described up until now have relied on the kinematical properties of x-ray diffraction that arise from the first Born approximation. This allowed us to use linear analysis techniques such as Fourier transformation. Here we will forego those advantages to make use of simple dynamical effects that can exaggerate the surface sensitivity. The relevant theory was first related to surface diffraction by Vineyard (1982) and developed further in the context of phase transitions by Dietrich and Wagner (1984). First-order perturbation theory is used to describe scattering within the classical total reflection situation and leads to a 'distorted-wave Born approximation'. We sometimes refer to the resulting characteristic diffraction features as 'Vineyard profiles'.

7.1. Basic formalism

The entire process is governed by the refractive index, n. Inside condensed matter at x-ray frequencies, n is slightly smaller than unity by about one part in 10^5. In general it is a complex quantity that accounts for both the change of group velocity

and photoelectric absorption of the x-ray wave inside a medium. It is usually expressed as

$$n = 1 - \delta - i\beta \tag{40}$$

with

$$\delta = \frac{\lambda^2}{2\pi}\frac{e^2}{mc^2}\frac{F(0)}{V} \tag{41}$$

$$\beta = \lambda\mu/4\pi \tag{42}$$

where μ is the photoelectric absorption per unit length, $F(0)$ is the structure factor (in electrons) at zero q and V is the unit cell volume.

When an x-ray beam is incident upon a surface at grazing angles it is refracted in just the same way as light on entering a denser medium. The sign of the difference in index implies that an x-ray beam is steered away from the normal, rather than towards it as for a light beam. At sufficiently grazing incidence angles α_i (of order 0.2 to 0.5 degrees), the refracted beam cannot travel further inside the medium and so undergoes 'total external reflection' instead. The threshold angle is the critical angle for external reflection, or just 'critical angle' α_c. Below the critical angle the x-ray beam is reflected without transmission as from a mirror; above it propagation occurs. Both cases are described by the angle-dependent (complex) transmission coefficient $T(\alpha_i)$ of a dielectric boundary, obtained by matching the parallel components of the electric field vector (Born and Wolf 1986)

$$T(\alpha) = \frac{2\sin\alpha}{\sin\alpha + \sqrt{n^2 - \cos^2\alpha}}. \tag{43}$$

This describes the wave amplitude just inside the surface (dielectric boundary). The intensity seen in an experiment will therefore be modified by $|T(\alpha_i)|^2$ which is plotted for two cases at the top of figure 20. 'No absorption' refers to $\beta = 0$, while 'with absorption' has the value of β for gold, which is a typical dense solid.

7.2. Scattering depth

The incident wave vector $\boldsymbol{k}_i$ is also modified upon crossing the boundary. Its parallel components are unchanged, but its perpendicular component k_{iz} becomes complex due to refraction and absorption:

$$k_{iz} = \frac{2\pi}{\lambda}\sqrt{n^2 - \cos^2\alpha_i}. \tag{44}$$

In the case of no absorption, $\beta = 0$, k_{iz} switches from purely real to purely imaginary at the critical angle, defined by $\cos\alpha_c = n$. When the wave vector is imaginary it is called 'evanescent' because this causes the wave amplitude to decay exponentially with depth. Finite values of β have the effect of softening the switching: the propagating wave at $\alpha_i > \alpha_c$ has a small imaginary component describing the normal absorption process, while for $\alpha_i < \alpha_c$ there is always a real component as well. In either situation the penetration depth Λ_i is simply related to the imaginary part of k_{iz} by

$$\Lambda_i = 1/\mathrm{Im}(k_{iz}). \tag{45}$$

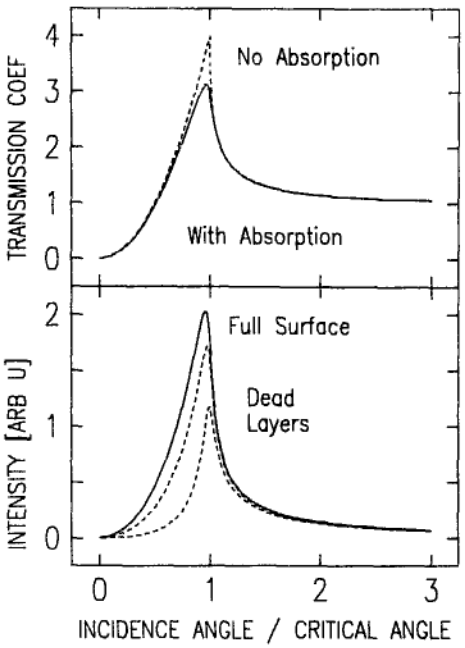

Figure 20. (*a*) Calculated transmission coefficient $|T|^2$ for x-rays crossing a dielectric boundary at grazing angle α_i, expressed as a multiple of α_c. (*b*) Vineyard profiles of in-plane bulk Bragg peaks calculated for gold at $\lambda = 1.5$ Å using equations (50) and (51). The upper dashed curve is for 5 Å of dead layers, the lower 20 Å.

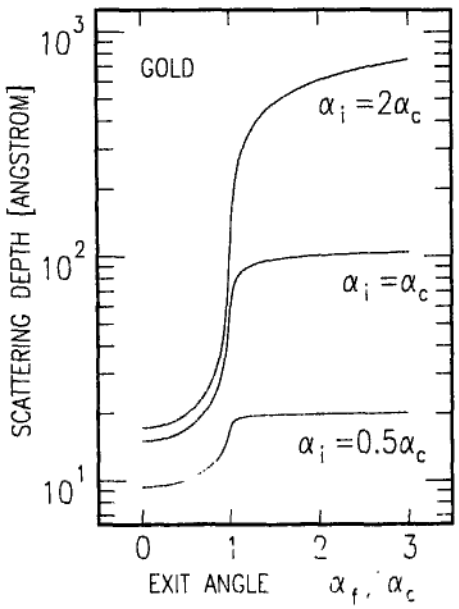

Figure 21. Universal curves of the variation of scattering depth Λ with incidence and exit angles α_i and α_f, expressed as multiples of α_c. The units of the vertical scale depend in general on the photoelectric absorption of the sample, but have been calculated here for gold at $\lambda = 1.5$ Å using equation (48).

For small incidence angles, this characteristic depth is small and increases with angle according to the universal curve of figure 21.

Before we can describe how this affects the diffracted intensity, we must consider the wave leaving the surface, k_f. This is easy because it behaves exactly the same as k_i due to time-reversal symmetry. Thus a beam emerging from the surface at exit angle α_f must have had a perpendicular wave vector inside the medium of

$$k_{fz} = \frac{2\pi}{\lambda}\sqrt{n^2 - \cos^2 \alpha_f}. \tag{46}$$

The exit beam distribution coming from the sample therefore probes a range of characteristic depths Λ_f given by

$$\Lambda_f = 1/\mathrm{Im}(k_{fz}). \tag{47}$$

Furthermore, the intensity distribution of the outgoing beam is also modified by $|T(\alpha_f)|^2$, where $T(\alpha)$ is the transmission coefficient of the dielectric boundary given by equation (43).

The diffraction profiles are always derived as functions of the momentum transfer $q = k_f - k_i$, which has a perpendicular component inside the crystal $q_z = k_{fz} - k_{iz}$ that depends on α_i and α_f via equations (44) and (46). Since q_z is a complex quantity, it also has the evanescent property and allows us to define a characteristic 'scattering depth' Λ that also depends on both α_i and α_f (Dosch 1987):

$$\begin{aligned}\Lambda &= 1/\mathrm{Im}(q_z) = 1/\mathrm{Im}(k_{fz} - k_{iz}) \\ &= \frac{\Lambda_i \Lambda_f}{\Lambda_i + \Lambda_f}.\end{aligned} \tag{48}$$

The scattering depth is a fundamental parameter that allows control of the depth of sample contributing to a given measurement. It can be systematically varied using α_i or α_f (or both) to perform depth-sensitive experiments, as shown in figure 21. The range of values attainable in practice is approximately 10 to 5000 Å depending on the material. While it is impossible to isolate a single layer in this way, it gives us a very useful range for the study of surface-induced phenomena (see below).

7.3. Vineyard profiles

Finally we can calculate the shape of an in-plane Bragg peak under grazing incidence/exit conditions, which is the Vineyard profile referred to above. If the derivation of the crystal truncation rod is carried out with complex q_z, the result will hold for all values of q_z because the attenuation due to absorption is automatically taken care of. Summing only along the z direction over layers separated by $a_3 = |a_3|$, as in equation (19),

$$\begin{aligned}F(q_z) &= \sum_{j=0}^{\infty} \exp(-\mathrm{i}q_z a_3 j) \\ &= \frac{1}{1 - \exp(-\mathrm{i}q_z a_3)}\end{aligned} \tag{49}$$

giving an intensity profile

$$I(q_z) = |T(\alpha_i)|^2 |T(\alpha_f)|^2 \frac{1}{|1 - \exp(-\mathrm{i}q_z a_3)|^2}. \tag{50}$$

This is the function plotted at the bottom of figure 20 denoted 'full surface'. Here we have calculated the curve for gold with $\alpha_i = 1.5\alpha_c$, but the full series has been obtained by Mailander *et al* (1990) for other values of α_i. These all have the characteristic skewed shape of surface modified Bragg peaks. The maximum of intensity is substantially shifted from $q_z = 0$, which corresponds to $\alpha_i = \alpha_f = 0$ for an in-plane Bragg peak, to a position closer to the critical angle α_c. This is a clear indication of refraction.

The broken curves at the bottom of figure 20 show the effect of p 'dead layers' that do not contribute to the diffraction:

$$F'(q_z) = \sum_{j=p}^{\infty} \exp(-iq_z a_3 j)$$

$$= \frac{\exp(-iq_z a_3 p)}{1 - \exp(-iq_z a_3)} \tag{51}$$

giving rise to the intensity profiles indicated. These were calculated for gold with firstly 5 Å then 20 Å not contributing. The dead layers participate in the absorption of the evanescent wave through the exponential part of the numerator in equation (51). This has a dramatic effect on the leading edge of the Vineyard profile where the scattering depth is still quite small. Conversely, if the falling edge is attenuated this must be due to roughness of the surface (Dosch *et al* 1991b). The Vineyard profile is then modified in a way analogous to equation (23).

The Vineyard profile of a purely surface diffraction feature (as opposed to an in-plane bulk Bragg peak) is the $|T(\alpha_i)|^2|T(\alpha_f)|^2$ function taken from equation (50) times the structure factor squared, which is approximately constant over the small range of q_z. When a wide detector slit is used, the α_f resolution becomes broadened and the $|T(\alpha_f)|^2$ variation is integrated away. This applies to CTR features associated with out-of-plane Bragg peaks or surface superstructure peaks such as the half-orders of W(100) in figure 18 where the $|T(\alpha_i)|^2$ variation is clearly seen.

7.4. Examples of the evanescent wave method

The evanescent wave surface diffraction technique has been used to study defect distributions and implantation profiles in the surface region of silicon. Because Si diffracts as a perfect crystal, Bernhard *et al* (1987) found it necessary to include the dynamical aspects of the problem. The dynamical theory of diffraction under grazing incidence conditions has also been considered by Aleksandrov *et al* (1984),Cowan *et al* (1986) and Hashizume and Sakata (1989). The dynamical versions of the α_f profiles look very much like those of figure 20, but have subtle differences. When a Si sample is implanted with charged ions, the energy deposited gives rise to an amorphized layer. When this is present it affects the profile by introducing dead layers, as we saw in equation (51). In addition, there is the possibility of residual crystalline material at the surface. The result is α_f profiles, such as that shown in figure 22, containing oscillations of intensity due to beating of these two components (Wallner *et al* 1988, 1989, Rugel *et al* 1992).

The analysis of α_f profiles as a function of temperature has been used by the group of Dosch *et al* (1986, 1988, 1991a, b) as a powerful way to study surface phase transitions (see also the next section). The phase transition, for example, might be between two structures, order–disorder or even melting. According to theory, such as

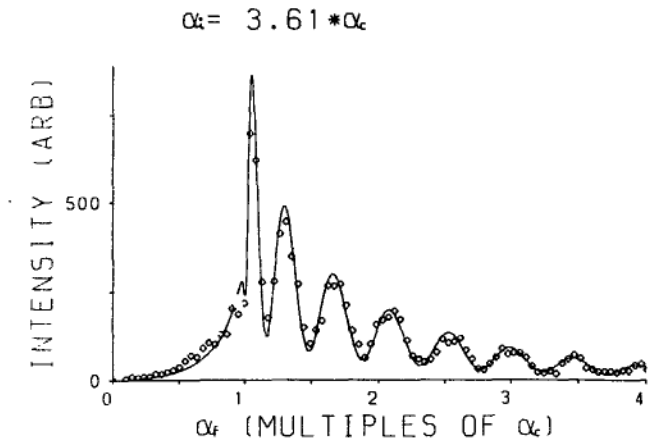

Figure 22. α_f profile of the in-plane 220 reflection of a Si(100) sample implanted with 10^{15} 100 keV Si^+ ions per cm^2. The sample was subsequently annealed at 630° C for 10 s, which led to partial recrystallization. The oscillations of intensity arise from interference between a thin (about 100 Å) surface slab of crystalline Si and the substrate, separated by about 1000 Å of amorphized material. Reproduced from Rugel *et al* (1992).

that explained by Lipowsky and Speth (1983), a phase transition in the bulk can be modified at the surface in a variety of ways, leading to a characteristic depth profile of the order parameter associated with the transition. This depth profile varies with temperature in a characteristic way as well. Following Dietrich and Wagner (1983, 1984), Dosch (1987) has derived a general formalism for analysing these profiles. Mailander *et al* (1990) and Dosch *et al* (1991b) have shown agreement with the theory of Lipowsky and Speth (1983) for the Cu_3Au order–disorder transition at the (100) surface. Dosch *et al* (1991a) have examined the surface melting of Al(110) in the same way.

In general it is possible to vary either the incidence or exit angle independently of the point in reciprocal space being measured. Vlieg *et al* (1987) showed how to do this with the five-circle diffractometer. For example, if α_i is varied, the cut direction of the sample and the reciprocal space point will fix α_f. When this is done, it does not matter whether a surface or bulk feature is being probed; the signal is proportional to $|T(\alpha_i)|^2|T(\alpha_f)|^2$ and depends on the scattering depth which is known from equation (48) or from the universal curve in figure 21.

This method was used by Zhu *et al* (1990a) to search for surface-region modification of the charge density wave (CDW) in $K_{0.3}MoO_3$. The CDW is incommensurate and appears below a second-order phase transition at 175 K. Neither the amplitude nor the incommensurate period was found to change near the surface, however, so it was concluded that the CDW exists at least to within 5 Å of the surface.

8. Lineshape analysis

This final method is going to lead away from details of structures at the atomic level towards questions of surface structure in the sense of morphology and its statistical representation. Important questions concerning the thermodynamics of surfaces can thereby be answered. Instead of performing crystallographic analysis we are going to see what information can be derived from examining the shape of the diffraction

peaks parallel to the surface, obtained by scanning the momentum transfer along the in-plane direction, which we generally denote $q_{\|}$. By convention we define $q_{\|} = 0$ at the position of the Bragg peak. Up until now, we have considered our surface diffraction peaks to be perfect δ functions in the $q_{\|}$ direction. However, this is only true if the surface structure is perfectly periodic across the entire sample with no defects, dislocations, domain boundaries, etc. Such a surface would be said to have correlations of infinite range. If a surface is poorly correlated, the peaks will be broadened. Here we discuss how we should analyse these peak shapes.

8.1. Correlation function

Recall equations (31) and (32), which discussed the Patterson function, $P(\boldsymbol{r})$. These showed that $P(\boldsymbol{r}) = \langle\rho(\boldsymbol{r})\rho(0)\rangle$, the unit cell electron density–density correlation function. There $P(\boldsymbol{r})$ was obtained by taking the Fourier transform of all the $|F_{hkl}|^2$, assuming these to correspond to ideal δ-function peaks. When the peaks are no longer ideally sharp this Fourier sum (equation (31)) must be replaced by the Fourier integral. This is then conventionally called $C(\boldsymbol{r})$, the electron density–density correlation function,

$$C(\boldsymbol{r}) = \langle\rho(\boldsymbol{r})\rho(0)\rangle$$
$$= \int I(\boldsymbol{q}) \exp(-\mathrm{i}\boldsymbol{q}\cdot\boldsymbol{r})\, \mathrm{d}^3q \tag{52}$$

where we have chosen to ignore the proportionality constant in the second relation for convenience. We are only interested in the large-r limit of $C(\boldsymbol{r})$, when the q integral is just over a small region in reciprocal space around the peaks. In this limit we can ignore the overlap with surrounding peaks and, since they will all have the same shape, we only need to consider one. Consequently, by taking the Fourier transform of a lineshape parallel to the surface, $I(q_{\|})$, we will obtain the correlation function for the surface in that particular direction. For example, if the correlation function is a Gaussian of width σ, the lineshape will also be a Gaussian with width $1/\sigma$; if the correlation function is a two-dimensional exponential $\exp(-|r|/\xi)$ with a characteristic length ξ, the lineshape will be a Lorentzian raised to the power $\frac{3}{2}$, $(1 + \xi^2 q_{\|}^2)^{-3/2}$, with width $1/\xi$. The characteristic decay distance of $C(r)$ is called the correlation length, and is usually denoted ξ. We now have a language suitable for talking about the diffraction associated with disordered systems and surface phase transitions.

Figure 23 depicts what is meant by the correlation function for the specific case of a surface broken into domains of average size ξ. Within each domain the surface is well ordered and so has $C(r) \sim 1$ for $r \ll \xi$. However, domains are separated by boundaries called domain walls, shaded in the figure. Each domain wall has a specific structure such as a step, a change of unit cell registration (called a phase boundary, typically 'antiphase') or a reorientation of the axes of the reconstructed unit cell. This results in adjacent domains being badly correlated or uncorrelated with respect to each other, giving $C(r) \sim 0$ for $r \gg \xi$. This explains the general trend of the correlation functions sketched in figure 23.

8.2. W(100) surface phase transition

Our example comes again from the W(100) surface. In figure 24 a top view of both the $\sqrt{2} \times \sqrt{2}$ reconstruction and the relevant section of reciprocal space are shown.

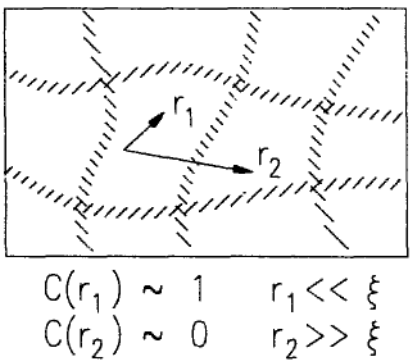

Figure 23. Visualization of the correlation function for the case of a surface broken into domains of average size ξ. The shaded lines represent domain walls.

The spots represent slices across the truncation rods while the ellipses represent the fractional order peaks due to the reconstruction. If scans were taken along the $q_{\parallel}$ and $q_{\perp}$ directions, as defined by the arrows, the order perpendicular and parallel to the chains of atoms would be probed. Such lineshapes were measured as functions of temperature by Robinson *et al* (1989b) and are plotted in figure 25. At low temperatures we see a sharp peak, indicating that the surface has very large regions of ordered $\sqrt{2} \times \sqrt{2}$ structure. As the temperature increases this peak becomes lower in height and broader in both directions, $q_{\parallel}$ and $q_{\perp}$, parallel and perpendicular to the total momentum transfer, $\boldsymbol{Q}$. The most important result here is that the *integrated* intensity, integrated under the 2D peak, is constant with temperature above and below the transition. Since this quantity is proportional to $|F_{hkl}|^2$, we conclude the local structure does not change at the transition. This is the chief characteristic of an order–disorder transition.

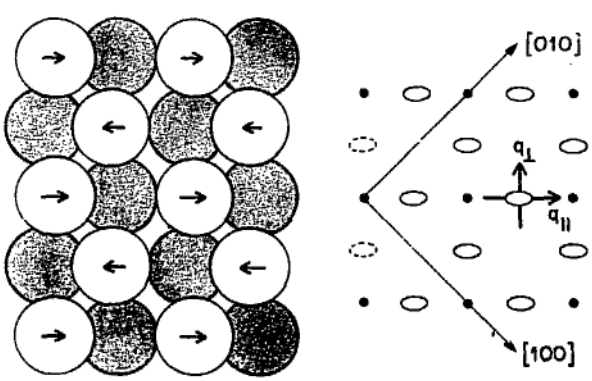

Figure 24. Atomic model and diffraction pattern of the low-temperature $\sqrt{2} \times \sqrt{2}$ reconstruction of W(100). Bulk diffraction peaks, e.g. (000), (020), (110) and (200), are full circles, and the half-order peaks unique to the reconstructed layer are ellipses. Integer-order surface peaks are not shown. Top-layer atoms (unshaded) are displaced as indicated to form zig-zag chains oriented up and down in the figure. The displacements of the second-layer atoms (shaded) are not shown. Measurements were made of the $(\frac{3}{2}, \frac{3}{2}, 0)$ peak, with $q_{\parallel}$ and $q_{\perp}$ defining the radial and transverse scan directions employed.

Such an order–disorder transition can be viewed therefore as conserving the local atomic arrangement, while changing the length scale over which it is ordered. Micro-

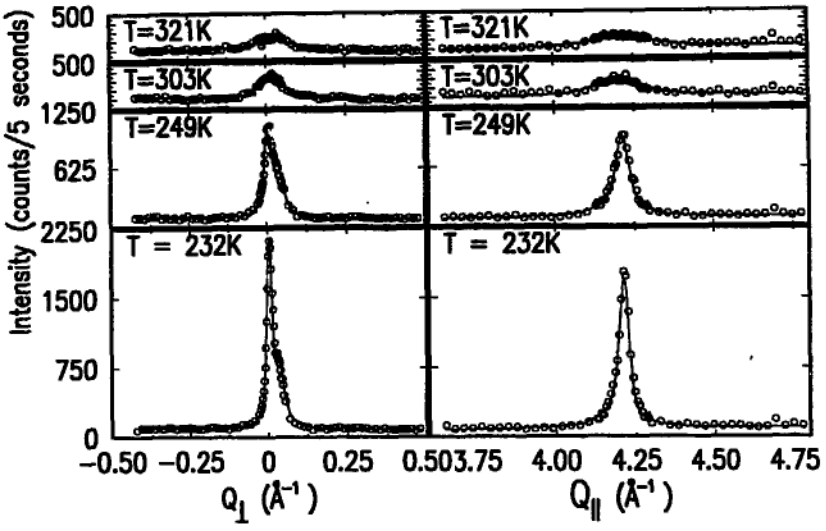

Figure 25. Radial ($Q_\parallel$) and transverse ($Q_\perp$) momentum transfer profiles of the $(\frac{3}{2}, \frac{3}{2}, 0)$ surface peak at various temperatures in the transition region for the W(100) surface of figure 24.

scopically the surface still looks like figure 24, but the scale of the macroscopic domain structure in figure 23 is changing with T. Here there are two correlation lengths $\xi_\parallel$ and $\xi_\perp$ corresponding to the two directions. These change dramatically from about 200 Å at low temperature to about 10 Å at high temperature, while remaining in about the same ratio to each other. The low-T limit is probably constrained by defects in the surface, while the high-T limit is determined only by the ability to detect such broad low peaks with x-rays. Probes which are more surface-sensitive, such as He scattering, can indeed follow the peak to much higher temperatures (Ernst *et al* 1987).

8.3. Examples of experiments using lineshape analysis

Surface phase transitions are widespread in overlayer systems. Traditionally studied were adsorbed gases, particularly noble gases, on graphite (Horn *et al* 1978, McTague *et al* 1982). Here the experiments were performed on powders or oriented powdered substrates, but considerable information was obtained with the high resolution of synchrotron x-ray diffraction. More recently, single crystal substrates have been employed so that phase transitions involving *rotation* of the overlayer could be examined (D'Amico *et al* 1984) that had previously been observed in LEED.

There have been a number of phase transitions seen in reconstructed clean metal surfaces other than W(100). The rotated hexagonal top layer of Au(100), which we met earlier, loses its rotation at 970 K and has a further disordering transition at 1170 K (Mochrie *et al* 1990). Pt(100) has similar phase transitions with an important difference that the rotation transition is second order (Abernathy *et al* 1992). Huang *et al* (1990) showed that Au(111) has an incommensurate hexagonal phase at room temperature that evolves gradually up to 865 K, then enters a discommensuration-fluid phase similar to that seen on Pt(111) at high temperature by Sandy *et al* (1991). At the electrochemical interface with an electrolyte, both Au(100) (Ocko *et al* 1990) and Au(111) (Wang *et al* 1992) undergo phase transitions as the applied potential is varied.

Au(110) (Held *et al* 1989) and Pt(110) (Robinson *et al* 1989c) have order–disorder transitions at 650 K and 1080 K, respectively. Because the elementary excitation that leads to disorder involves steps on the surface, the transition has a 'chirality' that gives rise to a shifting of the peak position. Such shifting was not observed in earlier LEED studies for example.

Phase transitions in metal overlayers have also been studied. Marra *et al* (1982) looked at Pb/Cu(110), while Lee *et al* (1990) looked at Pb/Cu(100). Grey *et al* (1989, 1990) looked at Pb/Ge(111). The kinetics of island growth of Co/Cu(100) were measured by Ferrer *et al* (1991). W(100) undergoes a series of coverage-dependent phase transitions upon dosing with hydrogen; these changes were elucidated by Chung *et al* (1987). Electrodeposited metallic layers have also been examined by Samant *et al* (1987) and found to compress under changes of applied potential.

The existence of surface melting transitions was proposed on theoretical grounds, for example by Lipowsky and Speth (1983). Depending on the relative free energies of the solid–liquid, liquid–vapour and solid–vapour interfaces, it can happen that a thin liquid layer is stable at a surface before the bulk melts. The clearest experimental indication is for Pb(110) studied by ion channelling by Frenken *et al* (1985) and Pluis *et al* (1987). Surface melting has also been established in freely suspended liquid crystal films by Swanson *et al* (1989) and in physisorbed noble gas films by Zhu and Dash (1988). Several surfaces have been examined with x-ray diffraction to look for evidence of this: Pb(110) by Fuoss *et al* (1988) and by Gay *et al* (1989); Al(110) by Dosch *et al* (1991b).

Surface modification of other first-order bulk phase transitions has been looked for near $Cu_3Au(111)$ surfaces by Zhu *et al* (1988, 1990b), in addition to the work of Mailander *et al* (1990) and Dosch *et al* (1991b) on $Cu_3Au(100)$.

Lineshape analysis is a powerful way of understanding surface morphology, as we will see in the next section. Renaud *et al* (1991) studied $Si(100)/SiO_2$ interfaces and found multiple peak strucures at the truncation rod positions. This was interpreted as due to the presence of interfacial steps in an ordered array.

8.4. Roughening transitions

Another kind of phase transition, unique to surfaces, is called a roughening transition. In the simplest case a surface can change from smooth at low T to become rough at high T. Such a transition can be driven by other means, such as chemical modification by adsorption, or could indeed occur at an interface.

One kind of roughening transition believed to apply to metal surfaces at elevated temperatures is called 'step roughening' and is illustrated schematically in figure 26. For $T \ll T_R$, the so-called roughening temperature, the surface has the regular array of steps shown in the upper panel. The crystal is imagined to be made up of cubes representing the atoms or unit cells. At high temperatures, $T \sim T_R$, the surface can lower its free energy by introducing fluctuations in the position of the steps as shown in the lower panel. By adopting a large number of configurations it increases its entropy and lowers its free energy. This only happens at sufficiently high temperatures that the energy cost of all the corners ('kinks') created is smaller than the entropy term.

8.4.1. Theoretical lineshape for a rough surface. We now consider how lineshape analysis of the diffraction from surfaces can identify whether a surface is in the rough or smooth state. The surface gives rise to truncation rods (CTRs) that emerge from each

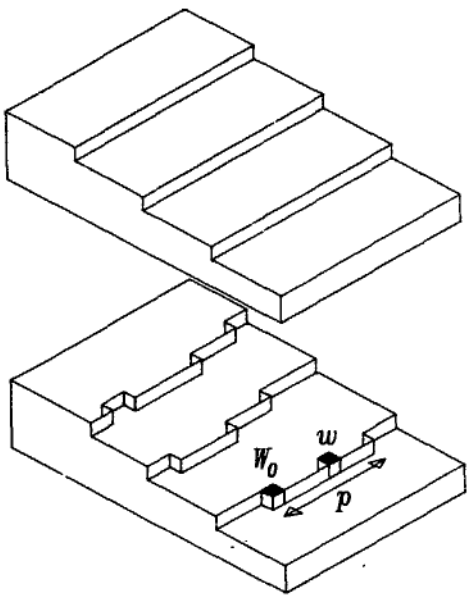

Figure 26. Morphology of a surface undergoing step roughening. Top: zero temperature ordered structure. Bottom: rough phase above the roughening temperature showing meandering steps.

bulk Bragg peak in the perpendicular direction. The regular step array with a uniform discrete number of atomic spacings on each terrace can be shown to have CTRs that join together to make continuous rods, just as we saw in equation (21). A slice through reciprocal space parallel to the surface will appear to have superlattice peaks spaced apart by the reciprocal of the distance between the steps. This is illustrated for an FCC (113) surface in figure 27. We have already seen in equation (23) the sensitivity of the *intensity* of the CTR to roughness (Robinson 1986). Here roughness implies *uncorrelated* roughness due to the statistical absence of atoms from sites in the surface. It is clear from figure 27 that a more general description is possible, whereby correlated fluctuations in the step positions will result in uncertainty in the effective direction of the surface normal, leading to a broadening of the rods into swathes.

The atomic model we will use to derive the general form of diffraction from a rough surface is the solid-on-solid (SOS) model. Here an ideal bulk lattice is assumed to be without distortions. The lattice of any low-index surface can transformed into one with a perpendicular z direction by a suitable choice of new lattice parameters a_1 and a_2 parallel to and a_3 perpendicular to the surface, as illustrated in figure 27(a). All the information about the morphology of the surface is contained in the envelope function that truncates this lattice. This is denoted as a discrete vertical height $h(x, y)$ for every discrete lateral site (x, y) and is assumed to be single valued everywhere, which excludes overhangs. Without loss of generality we can write $h(x)$ where x represents *both* in-plane directions. The kinematically scattered amplitude is then the sum of all atoms on the lattice within this boundary,

$$F(q_x, q_z) = \sum_{x=1}^{N} \sum_{z=-\infty}^{h(x)} \exp(\mathrm{i}(q_x a_1 x + q_z a_3 z))$$

$$= \sum_{x=1}^{N} \exp(\mathrm{i}(q_x a_1 x + q_z a_3 h(x))) \sum_{z'=-\infty}^{0} \exp(\mathrm{i} q_z a_3 z') \quad (53)$$

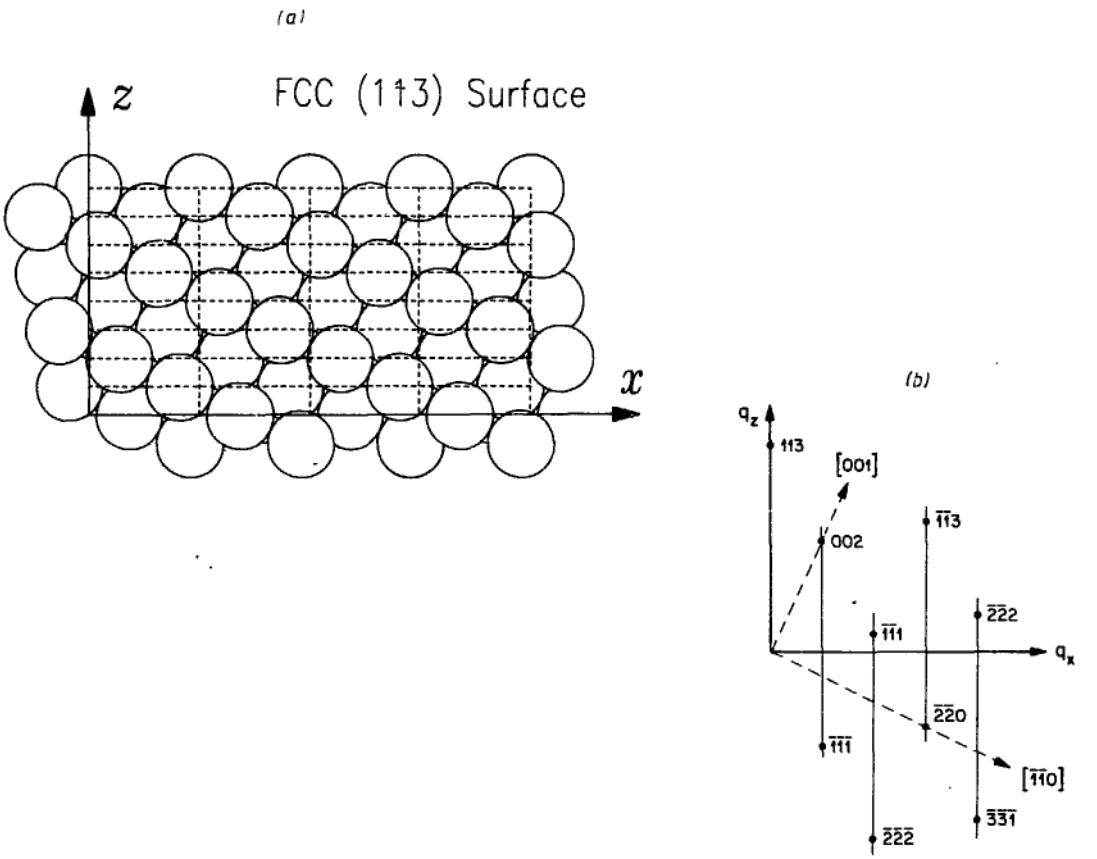

Figure 27. (*a*) Atomic model of a face-centred cubic crystal cut to expose its (113) surface. The coordinates are defined, as is customary, with the z direction along the normal. (*b*) The diffraction pattern of this object. The dots are bulk Bragg peaks indexed according to the bulk Miller index notation. The lines are the crystal truncation rods which follow the surface normal direction, but join together the bulk Bragg peaks and give rise to superlattice peaks in the q_x direction.

where a_1 and a_3 are the lattice parameters and N is the lateral size of the sample. The last summation in equation (53) is the familiar sum over layers that gives rise to the normal CTR form which we met in equations (19) and (49). It is written as the sum of a complex geometric series, with the usual caveat about it being the limit of a sum with a small real exponent representing absorption (see section 3.1),

$$F(q_x, q_z) = \sum_{x=1}^{N} \exp(\mathrm{i}(q_x a_1 x + q_z a_3 h(x))) \frac{1}{1 - \exp(-\mathrm{i} q_z a_3)}. \quad (54)$$

The diffracted intensity I is $\langle FF^* \rangle$ ensemble-averaged over all height configurations,

$$I(q_x, q_z) = \left\langle \sum_{xx'=1}^{N} \exp(\mathrm{i} q_x a_1 (x - x')) \exp(\mathrm{i} q_z a_3 (h(x) - h(x'))) \right\rangle \times \frac{1}{2 \sin^2(q_z a_3/2)}. \quad (55)$$

The surface can now be assumed to have the stationary property $h(x) - h(x') = h(\xi) - h(0)$ where $\xi = x - x'$, meaning it is the same everywhere on average, independent of the choice of origin.

$$I(q_x, q_z) = \sum_{\xi=1}^{N} \exp(iq_x a_1 \xi) \langle \exp(iq_z a_3 (h(\xi) - h(0))) \rangle \frac{1}{2\sin^2(q_z a_3/2)}. \tag{56}$$

The ensemble average in equation (56) has been evaluated by Villain *et al* (1985) and by Robinson *et al* (1990a) for the case where the height function $h(x)$ is a discrete Gaussian random variable with a sufficiently wide distibution. This gives us the following final expression for the diffraction lineshape of a rough surface:

$$I(q_x, q_z) = \sum_{\xi=1}^{N} \exp(iq_x a_1 \xi) \exp(-\langle (h(\xi) - h(0))^2 \rangle a_3^2 [q_z]^2/2) \frac{1}{2\sin^2(q_z a_3/2)} \tag{57}$$

where $[q_z]$ means q_z *modulo* $2\pi/a_3$ such that $-\pi/a_3 < [q_z] < \pi/a_3$. This quantity enters because it is the *nearest* Bragg peak that dominates the observed lineshape; a correction of a factor 2 in intensity is needed for the worst case $[q_z] = \pi/a_3$ because two Bragg peaks are equally important there.

Equation (57) can be thought of as the product of two terms: the second is the conventional CTR depending only on q_z, while the first describes its cross-sectional profile in q_x. By analogy with equation (52), we see that the first term is just the Fourier transform of an effective correlation function $C(\xi)$,

$$C(\xi) = \exp(-\langle (h(\xi) - h(0))^2 \rangle a_3^2 [q_z]^2/2). \tag{58}$$

We say *effective* because it is a correlation function that depends on the diffraction conditions through $[q_z]$. Thus the lineshape is derived in two steps from the statistical quantity $\langle (h(\xi) - h(0))^2 \rangle$ representing the roughness: first by forming the Gaussian quantity $C(\xi)$, then by Fourier transformation.

8.4.2. Examples of calculated profiles. Figure 28 shows graphically the evaluation of equation (57) for various height–height correlation functions $\langle (h(\xi) - h(0))^2 \rangle$ corresponding to different kinds of rough surface. Figure 28(*a*) has linear divergence of $\langle (h(\xi) - h(0))^2 \rangle$ with distance ξ, giving rise to a Lorentzian lineshape. The steeper the divergence with ξ is, the broader the resulting Lorentzian becomes. Since the Lorentzian width is proportional to $[q_z]^2$, the rod is narrow close to a Bragg peak and gets rapidly broader with distance.

Figure 28(*b*) corresponds to the *statistically* rough surface we met on the left of figure 5 and in section 3.2. In the strict language of roughening transitions we must now call this a *flat* surface, because its height fluctuations are bounded as ξ tends to ∞. On all distance scales there is a certain finite root mean square random (uncorrelated) height variation, h_0. $\langle (h(\xi) - h(0))^2 \rangle$ then has the constant value $2h_0$. This gives diffraction that is always sharp in cross section, as indicated by the δ function in q_x. The intensity along the rod varies with q_z according to

$$I(q_z) = \exp(-{h_0}^2 a_3^2 [q_z]^2) \frac{1}{2\sin^2(q_z a_3/2)}. \tag{59}$$

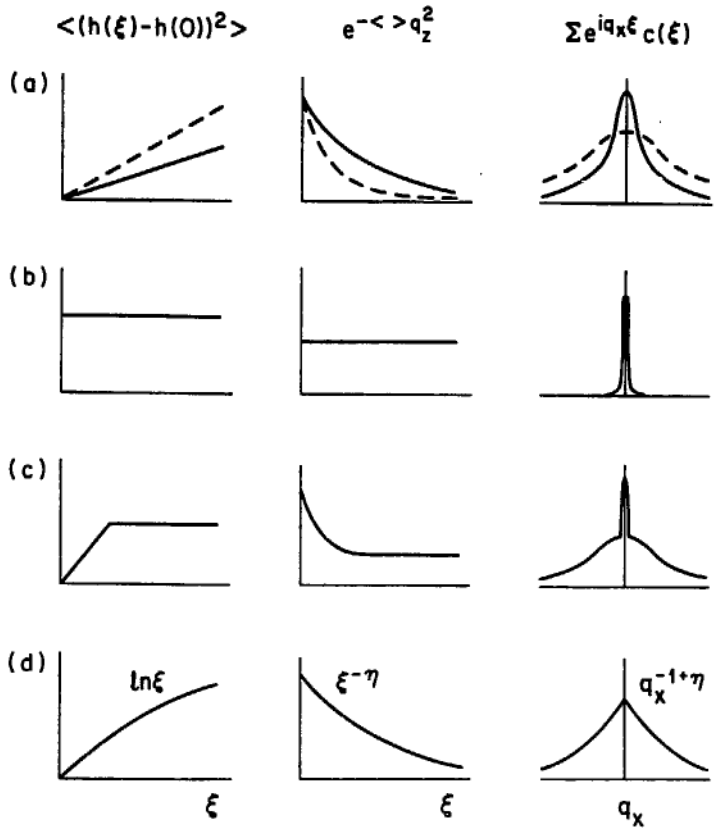

Figure 28. Cross-sectional lineshape of crystal truncation rods from a rough surface represented by different height–height correlation functions. The left column is the lateral dependence of the height–height correlation function. The middle column is the correlation function $C(\xi)$ obtained with equation (58). The right column is the Fourier transform of $C(\xi)$ which is the cross-sectional lineshape according to equation (57). From Robinson *et al* (1990a).

This is the standard CTR profile (equation (21)) multiplied by an effective Debye–Waller term (Warren 1969, Debye 1914) containing the roughness. This expression is an alternative to the form given in equation (23) for the exponential height distribution (Robinson 1986). They have very similar shapes that become identical in the limit of small roughness. The intensity also falls off faster than the ideal $1/[q_z]^2$. Equations (23) and (59) are both useful general formulae for obtaining a single measure of the RMS roughness h_0 from the intensity profile alone. Such a value should always be qualified with a lateral length scale: here it is the resolution of the instrument used. This measure of RMS roughness is meaningful only if the CTR cross section is seen to be resolution limited; otherwise it is not possible to use such a simple uncorrelated description and the details of the correlations must then be referred back to the original form of equation (57).

Figure 28(c) corresponds to an intermediate case with divergent correlations of height at short distance, switching over to saturation at large ξ with the value $2h_0$. The resulting lineshape is a composite of (a) and (b) with two components. When this situation is encountered in an experiment, the value of h_0 can then be extracted by subtraction of the broad component as part of the 'background' and proceeding with the analysis using equation (59).

8.4.3. Theories of roughening. The final row of figure 28(*d*) illustrates the case of *logarithmic* height divergence. This is expected for a rough surface of the kind described by the theory of Chui and Weeks (1976) for temperatures above the roughening transition. The lineshape has the characteristic *power-law* form shown, obtained by Fourier transformation of a correlation function with the algebraic decay form $C(\xi) \sim \xi^{-\eta}$. Because of its relation to a basic theory, many experiments have sought to verify the existence of this lineshape. However, it should be noted that the distinction between (*c*) and (*d*) is not that great, particularly when finite resolution, background and statistics of the intensity measurement are taken into account. Moreover functional forms intermediate between (*c*) and (*d*) could also be composed, for example without the sharp corner. The experimental distinction between rough and smooth boils down to whether the height diverges or remains finite as ξ tends to infinity; in the lineshape, we must decide whether or not there is a central δ function.

An alternative theory by Villain *et al* (1985) relates to the step roughening we saw in figure 26. Because the elementary excitation is a bound pair of kinks in the step edge bordering a terrace, it is sometimes referred to as a *terrace–step–kink* (TSK) model. The theory evaluates the statistical mechanics of a small density of such fluctuations in the ideal terrace structure as shown. Inspection of the (113) surface in figure 27(*a*) reveals that a sideways detour of a step results in an overall *vertical* change in height by one a_3 unit, which is some geometric fraction of the lattice spacing a_0. We consider that there are two important energies in the problem. One is the energy to form a kink, W_0, while the other is the energy to have one atom within a row of atoms displaced, w. These energies are illustrated in figure 26. It is assumed that $w \ll k_B T \ll W_0$. Consequently, the probability of an excitation of length p is just the Boltzmann factor $\exp(-(2W_0 + pw)/k_B T)$. We can then calculate the expectation value of the height fluctuation by just summing over all possible configurations, resulting in

$$\langle h^2 \rangle = \frac{\sum_{p=1}^{\infty} 2p \exp(-(2W_0 + pw)/k_B T)}{1 + 2\sum_{p=1}^{\infty} \exp(-(2W_0 + pw)/k_B T)}$$

$$= 2\left(\frac{k_B T}{w}\right)^2 \exp(-2W_0/k_B T). \tag{60}$$

ξ does not enter because no interaction between the fluctuations was assumed. The expectation value $\langle h^2 \rangle$ is simply substituted for h_0^2 in equation (59) to give us the variation of intensity along a CTR as a function of T,

$$I(q_z) = \exp(-2(k_B T/w)^2 \exp(-2W_0/k_B T) a_3^2 [q_z]^2) \frac{1}{2\sin^2(q_z a_3/2)}. \tag{61}$$

This is expected to work only at low temperatures when the excitations can be assumed to be infrequent and therefore non-interacting. Equation (61) would be expected to break down when T approaches T_R, as is found experimentally (Robinson *et al* 1990a).

8.4.4. Experimental work on roughening. We look first at examples of stepped surfaces where the theory of Villain *et al* (1985) might be expected to apply. The theory was originally developed for analysis of He diffraction data, and had already been seen

to explain data for stepped surfaces of Ni(115) by Conrad *et al* (1986), Ni(113) by Conrad *et al* (1987) and Cu(115) by Fabre *et al* (1987). It was first applied to the analysis of x-ray data for Cu(110) by Mochrie (1987), then to Cu(113) by Liang *et al* (1987, 1988) and Ni(113) by Robinson *et al* (1990a). We will use the Cu(113) data as our example, shown in figure 29.

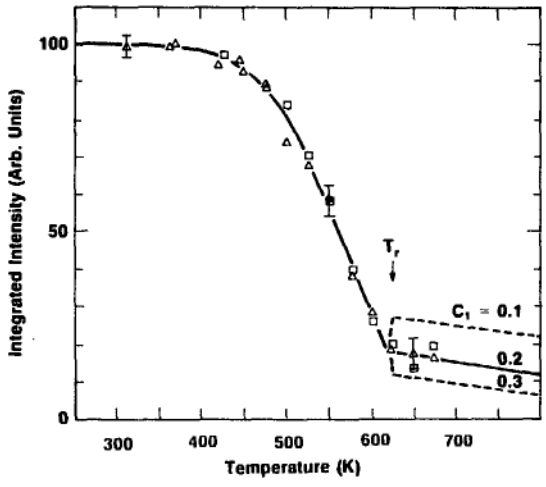

Figure 29. Roughening of Cu(113) as studied by Liang *et al* (1987). The integrated intensity of the step superlattice peak is plotted against temperature. Squares were taken on heating and triangles on cooling. Typical uncertainties are shown. The full curve is from equation (61) which is derived from Villain *et al* (1985).

The data show the integrated intensity measured at the point in figure 27(*b*) where the first CTR crosses the q_x axis. This corresponds to a value of $[q_z] = 10\pi/11a_3$, so it is very close to the CTR midpoint, or the so-called *anti-Bragg* postion $[q_z] = \pi/a_3$, where the diffraction is most sensitive to the roughness. The intensity drops abruptly with temperature, suggesting roughening with T_R about 620 K. The approach to roughening fits well to the TSK theory as shown, giving the values $W_0 = 2100$ K and $w = 65$ K consistent with the assumption that $w \ll k_B T \ll W_0$.

The study of Ni(113) by Robinson *et al* (1990a), when analysed with the same theory, gave the values $T_R = 740$ K, $W_0 = 3500$ K and $w = 55$ K, and the work on Cu(110) by Mochrie (1987) gave the values $T_R = 870$ K, $W_0 = 2260$ K and $w = 170$ K. The crystal used in the latter study was later found to have been miscut and was undergoing a facetting transition (see below), so that roughening (if any) of Cu(110) would actually take place at much higher temperatures (Ocko and Mochrie 1988). This resolved the apparent inconsistency with He scattering data for Cu(110) by Zeppenfeld *et al* (1989) which placed T_R above 900 K.

An example of a surface that disorders at high temperature without any observable change of lineshape is Ge(111), studied by Mak *et al* (1991). Here the uncorrelated roughness that leads to the drop of CTR intensity is due to a proliferation of vacancies associated with *sublimation*, which was confirmed by a rise of vapour pressure of Ge. Similar diffraction behaviour was seen on Ge(100) by Johnson *et al* (1991). Oscillatory changes in local roughness were seen during growth of Ge on Ge(111) by Vlieg *et al* (1988), caused by partial and complete filling of atomic layers. These are analogous to the oscillations seen in RHEED and the diffraction lineshape *versus* coverage can be understood in an analogous way (Vlieg *et al* 1989b).

Now we turn to roughening with the logarithmic height divergence as predicted by Chui and Weeks (1976). Held *et al* (1987) measured the shape of one of the CTRs of Ag(110) near the anti-Bragg position $[q_z] = \pi/a_3$ and found a lineshape suggestive of the power-law drawn in the bottom right of figure 28. As temperature was increased to around 750 K, the power-law exponent was found to climb from a small value to near unity. This was suggestive of roughening with $T_R = 723$ K.

The theory of diffraction from rough surfaces outlined above makes a clear prediction that the exponent η should be proportional to $[q_z]^2$. Robinson *et al* (1991) set out to verify this dependence for Ag(110) but found instead that, for their sample, as soon as they departed from $[q_z] = \pi/a_3$, the lineshape became split into two components with different centres. Since the power law cannot be asymmetric, this must be more like the case of figure 28(*c*), not (*d*). It is clear from figure 27(*b*) that if two nearby facet orientations are simultaneously present we expect to see split CTRs. Since the two components must come from different parts of the sample, Robinson *et al* (1991) concluded that the Ag(110) surface had *phase separated* into rough and smooth regions with slightly different orientations. The relative areas of the two regions as well as the angle between them changed with temperature until the rough region had taken over the whole sample above the roughening temperature of $T_R = 790$ K. The value of T_R would be expected to be dependent on miscut orientation.

This microscopic facetting into 'hill and valley' structures was originally proposed by Herring (1951). Wortis (1988) showed that such behaviour would be expected under certain conditions from consideration of the equilibrium crystal shape. This is the same behaviour seen by Ocko and Mochrie (1988) for Cu(110) that we mentioned above. Reversible facetting was also studied systematically on Si(111) vicinal surfaces by Phaneuf *et al* (1988) using LEED and by Noh *et al* (1991) using x-rays. Shen *et al* (1990) made an x-ray study of a Ni(111) vicinal.

Very recently Abernathy *et al* (1992a) have studied Pt(100) at high temperature and concluded that it roughens at around 1800 K. Above T_R they saw the power-law lineshape indicative of logarithmic divergence of $\langle (h(\xi) - h(0))^2 \rangle$, and most importantly they saw the quadratic dependence of the exponent η upon $[q_z]$. No details of the roughening transition itself are yet available.

Thus we have seen that there are at least three kinds of rough surface and corresponding roughening transitions that can occur: the statistically rough surface of Cu(113) without lateral correlations, the rough surface with logarithmic height divergence predicted by Chui and Weeks (1976) and now seen on Pt(100), and the inhomogeneous, microscopically facetted or phase separated case of Ag(110). Strictly, only surfaces with divergent height correlations can be considered rough; on these there is no δ-function component to the diffraction. Frequently the more widespread case of *local* roughness (figure 28(*b*) or (*c*)) is included in the definition, even though such surfaces are flat in the long range.

The microscopic difference in origin of these classifications lies in the relative free energies of terraces, steps and kinks and interactions between them. On the macroscopic scale, some of the behaviour can be understood from the surface tension versus orientation, through the equilibrium crystal shape (Wortis 1988). To observe the differences it is clear that high-resolution measurements of x-ray diffraction lineshapes can play an important role. Presently this is a fairly young field and it is to be expected that more developments will take place in the future.

9. Future outlook

There are two central reasons we believe surface x-ray diffraction has a bright future. The first is the confidence that the 60 years of service paid by conventional bulk x-ray diffraction to most branches of physics and chemistry can be carried over to surfaces and interfaces. There is a general trend towards more and more microscopic length scales that inevitably makes surfaces and their properties more important. This is as true in the materials science of semiconductor devices as it is in low-temperature physics or electrochemistry. It is also apparent that chemical reactions at interfaces can be understood and mastered to engineer materials at the atomic level, such as Langmuir–Blodgett films or self-assembled monolayer structures. The techniques described in this review are ideal for the characterization of these problems. They make a perfect complement to the scanning tunnelling (STM) and atomic force microscopes, that are also now widely applied to these problems. While the STM can provide an overview of a structure, the diffraction experiment will yield the information at the atomic level.

The second reason is that we are in the midst of a revolution in x-ray sources. Fifteen years ago electron storage rings at LURE (Orsay) and SPEAR (Stanford), for example, started to receive parasitic users of synchrotron x-rays. Then came dedicated facilities like the National Synchrotron Light Source at Brookhaven, that were constructed to support user programs. The technical lessons learned there about preparation and customization of powerful x-ray beams is presently being applied to the construction of new third-generation facilities: the European Synchroron Radiation Source in Grenoble, the Advanced Photon Source at Argonne and SPring-8 in Osaka. Over the two decades since the debut of synchrotron radiation, the brightness of x-ray sources will have improved by at least six orders of magnitude. The view of the world of scientific possibilities from this new vantage point will be radically different.

References

Abernathy D L, Mochrie S G J, Zehner D M, Grubel G and Gibbs L D 1992 *Phys. Rev.* B **45**
—— 1992a to be published
Akimoto K, Mizuki J, Tatsumi T, Aizaki N and Matsui J 1987 *Surf. Sci.* **183** L297
Aleksandrov P A, Afanas'ev A M and Stepanov S A 1984 *Sov. Phys.–Crystallogr.* **29** 226
Altman M S, Estrup P J and Robinson I K 1988 *Phys. Rev.* B **38** 5211
Andrews S R and Cowley R A 1985 *J. Phys. C: Solid State Phys.* **18** 6247
Belzner A, Ritter E and Schulz H 1989 *Surf. Sci.* **209** 379
Bernhard N, Burkel E, Compper G, Metzger H, Peisl J, Wagner H and Wallner G 1987 *Z. Phys.* B **69** 303
Bevington P R 1969 *Data Reduction and Error Analysis for the Physical Sciences* (New York: McGraw-Hill)
Bohr J, Feidenhans'l R, Nielsen M, Toney M, Johnson R L and Robinson I K 1985 *Phys. Rev. Lett.* **54** 1275
Born M and Wolf E 1986 *Principles of Optics* 5th edn (New York: Pergamon)
Brennan S, Fuoss P H and Eisenberger P 1986 *Phys. Rev.* B **33** 3678
Chui S T and Weeks J D 1976 *Phys. Rev.* B **14** 4978

Chung J W, Evans-Lutterodt K, Specht E D, Birgeneau R J, Estrup P J and Kortan A R 1987 *Phys. Rev. Lett.* **59** 2192
Conrad E H, Allen L R, Blanchard D L and Engel T 1987 *Surf. Sci.* **187** 265
Conrad E H, Aten R M, Kaufman D S, Allen L S, Engel T, den Nijs M and Riedel E K 1986 *J. Chem. Phys.* **84** 1015
Conway K M, Macdonald J E, Norris C, Vlieg E and van der Veen J F 1989 *Surf. Sci.* **215** 555
Coulman D J, Wintterlin J, Behm R J and Ertl G 1990 *Phys. Rev. Lett.* **64** 1761
Cowan P L, Brennan S, Jach T, Bedzyk M J and Materlik G 1986 *Phys. Rev. Lett.* **57** 2399
Cowley R A and Lucas C 1989 *J. Physique Colloq.* **C7** 145
D'Amico K L, Moncton D E, Specht E D, Birgeneau R J, Nagler S E and Horn P M 1984 *Phys. Rev. Lett.* **53** 2250
Debe M and King D 1977 *Phys. Rev. Lett.* **39** 708
Debye P 1914 *Ann. Phys., Lpz.* **45** 49
Dietrich S and Wagner H 1983 *Phys. Rev. Lett.* **51** 1469
—— 1984 *Z. Phys.* B **56** 207
Ding Y G, Chan C T and Ho K M 1991 *Phys. Rev. Lett.* **67** 1454
Dosch H 1987 *Phys. Rev.* B **35** 2137
Dosch H, Batterman B W and Wack D C 1986 *Phys. Rev. Lett.* **56** 1144
Dosch H, Hofer T, Peisl J and Johnson R L 1991a *Europhys. Lett.* **15** 527
Dosch H, Mailander L, Lied A, Peisl J, Grey F, Johnson R L and Krummacher S 1988 *Phys. Rev. Lett.* **60** 2382
Dosch H, Mailander L, Reichert H, Peisl J and Johnson R L 1991b *Phys. Rev.* B **43** 13172
Eisenberger P and Marra W C 1981 *Phys. Rev. Lett.* **46** 1081
Ernst H J, Hulpke E and Toennies J P 1987 *Phys. Rev. Lett.* **58** 1941
Fabre F, Gorse D, Lapujoulade J and Salanon B 1987 *Europhys. Lett.* **3** 737
Feidenhans'l R 1989 *Surf. Sci. Rep.* **10** 105
Feidenhans'l R, Grey F, Bohr J, Nielsen M and Johnson R L 1989 *J. Physique Coll.* **C7** 175
Feidenhans'l R, Grey F, Johnson R L, Mochrie S G J, Bohr J and Nielsen M 1990a *Phys. Rev.* B **41** 5420
Feidenhans'l R, Grey F, Nielsen M, Besenbacher F, Jensen F, Laegsgaard E, Stensgaard I, Jacobsen K W, Norskov J K and Johnson R L 1990b *Phys. Rev. Lett.* **65** 2027
Feidenhans'l R, Nielsen M, Grey F, Johnson R L and Robinson I K 1987 *Surf. Sci.* **186** 499
Feidenhans'l R, Pedersen J S, Bohr J, Nielsen M, Grey F and Johnson R L 1988 *Phys. Rev.* B **38** 9715
Feidenhans'l R, Pedersen J S, Nielsen M, Grey F and Johnson R L 1986 *Surf. Sci.* **178** 927
Ferrer S, Vlieg E and Robinson I K 1991 *Surf. Sci.* **250** L363
Fery P, Moritz W and Wolf D 1988 *Phys. Rev.* B **38** 7275
Frenken J W M and van der Veen J F 1985 *Phys. Rev. Lett.* **54** 134
Fuoss P H and Brennan S 1990 *Ann. Rev. Mater. Sci.* **20** 365
Fuoss P H, Kisker D W, Brennan S, Kahn J L, Renaud G and Tokuda K L 1989a *J. Physique Colloq.* **C7** 159
Fuoss P H, Kisker D W, Renaud G, Tokuda K L, Brennan S and Kahn J L 1989b *Phys. Rev. Lett.* **63** 2389
Fuoss P H, Norton L J and Brennan S 1988 *Phys. Rev. Lett.* **60** 2046
Gay J M, Pluis B, Frenken J W M, Gierlotka S, van der Veen J F, Macdonald J E, Williams A A, Piggins N and Als-Nielsen J 1989 *J. Physique Colloq.* **C7** 289
Gibbs D, Grübel G, Zehner D M, Abernathy D L and Mochrie S G J 1991 *Phys. Rev. Lett.* **67** 3117
Gibbs D, Ocko B M, Zehner D M and Mochrie S G J 1988 *Phys. Rev.* B **38** 7303
—— 1990 *Phys. Rev.* B **42** 7330
Gossmann H J, Bean J C, Feldman L C and McRae E G 1984 *Surf. Sci.* **138** L175
Gossmann H J, Bean J C, Feldman L C, McRae E G and Robinson I K 1985 *Phys. Rev. Lett.* **55** 1106
Grey F and Feidenhans'l R 1988 *Europhys. News* **19** 94
Grey F, Feidenhans'l R, Nielsen M and Johnson R L 1989 *J. Physique Colloq.* **C7** 181
Grey F, Feidenhans'l R, Skov Pedersen J, Nielsen M and Johnson R L 1990 *Phys. Rev.* B **41** 9519
Grey F, Johnson R L, Pedersen J S, Feidenhans'l R and Nielsen M 1988 *The Structure of Surfaces* vol. II, ed J F van der Veen and M A van Hove (Berlin: Springer) p 292
Haneman D 1987 *Rep. Prog. Phys.* **50** 1045
Hashizume H and Sakata O 1989 *J. Physique Colloq.* **C7** 225
Hashizume H, Sugiyama M, Niwa T, Sakata O and Cowan P L 1992 *Rev. Sci. Instrum.* **63** 1142
Headrick R L, Feldman L C and Robinson I K 1989a *Appl. Phys. Lett.* **55** 442
Headrick R L, Robinson I K, Vlieg E and Feldman L C 1989b *Phys. Rev. Lett.* **63** 1253

Headrick R L, Wier B E, Bevk J, Freer B S, Eaglesham D J and Feldman L C 1990 *Phys. Rev. Lett.* **65** 1128
Held G A, Jordan-Sweet J L, Horn P M, Mak A and Birgeneau R J 1987 *Phys. Rev. Lett.* **59** 2075
—— 1989 *Solid State Commun.* **72** 37
Herring C 1951 *Phys. Rev.* **82** 87
Hirosawa I, Akimoto K, Tatsumi T, Mizuki J and Matsui J 1990 *J. Cryst. Growth* **103** 150
Horn P M, Birgeneau R J, Heiney P and Hammonds E M 1978 *Phys. Rev. Lett.* **41** 961
Huang K G, Gibbs D, Zehner D M, Sandy A R and Mochrie S G J 1990 *Phys. Rev. Lett.* **65** 3313
Ichikawa I and Ino S 1981 *Surf. Sci.* **105** 395
Iida Y, Shimura T, Harada J, Samata S and Matsushita Y 1991 *Surf. Sci.* **258** 235
Jackson J D 1975 *Classical Electrodynamics* (New York: Wiley)
Jedrecy N, Sauvage-Simkin M, Pinchaux R, Massies J, Greiser N and Etgens V H 1990a *J. Cryst. Growth* **102** 293
—— 1990b *Surf. Sci.* **230** 197
Johnson A D, Norris C, Frenken J W M, Derbyshire H S, Macdonald J E, van Silfhout R G and van der Veen J F 1991 *Phys. Rev.* B **44** 1134
Jona F, Strozier J A Jr and Yang W S 1982 *Rep. Prog. Phys.* **45** 527
Kashihara Y, Kawamura K and Harada J 1991 *Surf. Sci.* **257** 210
Kashiwagura N, Kashihara Y, Sakata M, Harada J, Wilkins S W and Stevenson A W 1987 *Japan. J. Appl. Phys.* **26** L2026
Kisker D W, Fuoss P H, Tokuda K L, Renaud G, Brennan S and Kahn J L 1990 *Appl. Phys. Lett.* **56** 2025
Lee C H, Sheu E Y, Liang K S, D'Amico K L and Unert'l W N 1990 *Appl. Phys.* A **51** 191
Liang K S, Fuoss P H, Hughes G J and Eisenberger P 1985 *The Structure of Surfaces* vol I, ed. M A van Hove and S Y Tong (Berlin: Springer) p 246
Liang K S, Sirota E B, D'Amico K L, Hughes G J and Sinha S K 1987 *Phys. Rev. Lett.* **59** 2447
Liang K S, Sirota E B, Hughes G J, D'Amico K L and Eisenberger P 1988 *Structure of Surfaces* vol. II, ed. J F van der Veen and M A van Hove (Berlin: Springer) p 509
Lipowsky R and Speth W 1983 *Phys. Rev.* B **28** 3983
Lipson H and Cochran W 1966 *The Determination of Crystal Structures* (Ithaca, NY: Cornell University Press)
Mailander L, Dosch H, Peisl J and Johnson R L 1990 *Phys. Rev. Lett.* **64** 2527
Mak A, Evans-Lutterodt K W, Blum K, Noh D Y, Brock J D, Held G A and Birgeneau R J 1991 *Phys. Rev. Lett.* **66** 2002
Marra W C, Eisenberger P and Cho A Y 1979 *J. Appl. Phys.* **50** 6927
Marra W C, Fuoss P H and Eisenberger P 1982 *Phys. Rev. Lett.* **49** 1169
McTague J P, Als-Nielsen J, Bohr J and Nielsen M 1982 *Phys. Rev.* B **25** 7765
Mizuki J, Akimoto K, Hirosawa I, Hirose K, Mizutani T and Matsui J 1988 *J. Vacuum Sci. Technol.* B **6** 31
Mochrie S G J 1987 *Phys. Rev. Lett.* **59** 304
—— 1988 *J. Appl. Cryst.* **21** 1
Mochrie S G J, Zehner D M, Ocko B M and Gibbs D 1990 *Phys. Rev. Lett.* **64** 2925
Moncton D E and Brown G S 1983 *Nucl. Instum. Methods* **208** 579
Moritz W and Wolf D 1979 *Surf. Sci.* **88** L29
—— 1985 *Surf. Sci.* **163** L655
Noh D Y, Blum K I, Ramstad M J and Birgeneau R J 1991 *Phys. Rev.* B **44** 10 969
Northrup J E 1984 *Phys. Rev. Lett.* **53** 683
—— 1986 *Phys. Rev. Lett.* **57** 154
Ocko B M, Gibbs D, Huang K G, Zehner D M and Mochrie S G J 1991 *Phys. Rev.* B **44** 6429
Ocko B M and Mochrie S G J 1988 *Phys. Rev.* B **38** 7378
Ocko B M, Wang J, Davenport A J and Isaacs H S 1990 *Phys. Rev. Lett.* **65** 1466
Ourmazd A, Fuoss P H, Bevk J and Morar J F 1989 *Appl. Surf. Sci.* **41** 365
Patterson A L 1934 *Phys. Rev.* **46** 372
Pedersen J S 1988 *PhD thesis* University of Copenhagen, Riso-M-Report 2713
Pedersen J S, Feidenhans'l R, Nielsen M, Grey F and Johnson R L 1988 *Phys. Rev.* B **38** 13210
Pedersen J S, Feidenhans'l R, Nielsen M, Kjaer K, Grey F and Johnson R L 1987 *Surf. Sci.* **189/190** 1047
Phaneuf R J, Williams E D and Bartelt N C 1988 *Phys. Rev.* B **38** 1984
Pluis B, Denier van der Gon A W, Frenken J W M and van der Veen J F 1987 *Phys. Rev. Lett.* **59** 2678
Renaud G, Fuoss P H, Ourmazd A, Bevk J, Freer B S and Hahn P O 1991 *Appl. Phys. Lett.* **58** 1044

Robinson I K 1983 *Phys. Rev. Lett.* **50** 1145
—— 1986 *Phys. Rev.* B **33** 3830
—— 1987 *Phys. Rev.* B **35** 3910
—— 1988a *Aust. J. Phys.* **41** 359
—— 1988b *J. Vacuum Sci. Technol.* A **6** 1966
—— 1989 *Rev. Sci. Instrum.* **60** 1541
—— 1991 *Handbook on Synchrotron Radiation* vol. 3, ed. D E Moncton and G S Brown (Amsterdam: North-Holland) p 221
Robinson I K, Bohr J, Feidenhans'l R, Nielsen M, Grey F and Johnson R L 1989a *Surf. Sci.* **217** L435
Robinson I K, Conrad E H and Reed D S 1990a *J. Physique* **51** 41
Robinson I K, MacDowell A A, Altman M S, Estrup P J, Evans-Lutterodt K, Brock J D and Birgeneau R J 1989b *Phys. Rev. Lett.* **62** 1294
Robinson I K, Tung R T and Feidenhans'l R 1988a *Phys. Rev.* B **38** 3632
Robinson I K, Vlieg E and Ferrer S 1990b *Phys. Rev.* B **42** 6954
Robinson I K, Vlieg E, Hornis H and Conrad E H 1991 *Phys. Rev. Lett.* **67** 1890
Robinson I K, Vlieg E and Kern K 1989c *Phys. Rev. Lett.* **63** 2578
Robinson I K, Waskiewicz W K, Fuoss P H and Norton L J 1988b *Phys. Rev.* B **37** 4325
Robinson I K, Waskiewicz W K, Fuoss P H, Stark J B and Bennett P A 1986b *Phys. Rev.* B **33** 7013
Robinson I K, Waskiewicz W K, Tung R T and Bohr J 1986b *Phys. Rev. Lett.* **57** 2714
Rugel S, Wallner G, Metzger H and Peisl J 1991 *Acta Crystal.* C
Samant M G, Toney M F, Borges G L, Blum L and Melroy O R 1987 *Surf. Sci.* **193** L29
Sandy A R, Mochrie S G J, Zehner D M, Grubel G, Huang K G and Gibbs D 1992 *Phys. Rev. Lett.* **68** in press
Sandy A R, Mochrie S G J, Zehner D M, Huang K G and Gibbs D 1991 *Phys. Rev.* B **43** 4667
Sauvage-Simkin M, Pinchaux R, Massies J, Claverie P, Jedrecy N, Bonnet J and Robinson I K 1989 *Phys. Rev. Lett.* **62** 563
Shen Q, Chang J P, Navrotski G and Blakely J M 1990 *Phys. Rev. Lett.* **64** 451
Swanson B D, Stragier H, Tweet D J and Sorensen L B 1989 *Phys. Rev. Lett.* **62** 909
Takahashi T, Izumi K, Ishikawa T and Kikuta S 1987a *Surf. Sci.* **183** L302
Takahashi T, Nakatani S, Ishikawa T and Kikuta S 1987b *Surf. Sci.* **191** L825
Takahashi T, Nakatani S, Okamoto N, Ishikawa T and Kikuta S 1988 *Japan. J. Appl. Phys.* **27** L753
Takahashi T, Takayama I, Ishikawa T, Ohta T and Kikuta S 1985 *Japan. J. Appl. Phys.* **24** L727
Takayanagi K, Tanishiro Y, Takahashi S and Takahashi M 1985 *Surf. Sci.* **164** 367
Tong S Y, Xu G and Mei W N 1984 *Phys. Rev. Lett.* **52** 1693
Vanderbilt D 1987 *Phys. Rev.* B **36** 6209
van Hove M A and Tong S Y 1979 *Surface Crystallography by LEED* (Berlin: Springer)
van Loenen E J, Frenken J W M, van der Veen J F and Valeri S 1985 *Phys. Rev. Lett.* **54** 827
van Silfhout R G, van der Veen J F, Norris C and Macdonald J E 1990 *Faraday Discuss. Chem. Soc.* **89** 169
Villain J, Grempel D R and Lapujoulade J 1985 *J. Phys. F: Met. Phys.* **15** 809
Vineyard G H 1982 *Phys. Rev.* B **26** 4146
Vlieg E, Denier van der Gon A W, van der Veen J F, Macdonald J E and Norris C 1988 *Phys. Rev. Lett.* **61** 2241
—— 1989a *Surf. Sci.* **209** 100
Vlieg E, Fischer A E M J, van der Veen J F, Dev B N and Materlik G 1986 *Surf. Sci.* **178** 36
Vlieg E, Robinson I K and Kern K 1990a *Surf. Sci.* **233** 248
Vlieg E, Robinson I K and McGrath R 1990b *Phys. Rev.* B **41** 7896
Vlieg E, van der Veen J F, Gurman S J, Norris C and Macdonald J E 1989b *Surf. Sci.* **210** 301
Vlieg E, van der Veen J F, Macdonald J E and Miller M 1987 *J. Appl. Cryst.* **20** 330
von Laue M 1936 *Ann. Phys., Lpz.* **26** 62
Wallner G, Burkel E, Metzger H and Peisl J 1988 *phys. status solidi* **108** 129
Wallner G, Burkel E, Metzger H, Peisl J and Rugel S 1989 *Mat. Res. Soc. Symp. Proc.* **143** 19
Wang J, Ocko B M, Davenport A J and Isaacs H S 1992 *Science* **255** 1416
Warren B E 1969 *X-ray Diffraction* (Reading, MA: Addison-Wesley)
Wells A F 1985 *Structural Inorganic Chemistry* (Oxford: Clarendon)
Wilson R J and Chiang S 1987 *Phys. Rev. Lett.* **59** 2329
Wortis M 1988 *Chemistry and Physics of Solid Surfaces* vol VII, ed. R Vanselow and R Howe (Berlin: Springer)

Zegenhagen J, Huang K G, Gibson W M, Hunt B D and Schowalter L J 1989 *Phys. Rev.* B **39** 10254
Zeppenfeld P, Kern K, David R and Comsa G 1989 *Phys. Rev. Lett.* **62** 63
Zhu D M and Dash J G 1988 *Phys. Rev. Lett.* **60** 432
Zhu X M, Feidenhans'l R, Zabel H, Als-Nielsen J, Du R, Flynn C P and Grey F 1988 *Phys. Rev.* B **37** 7157
Zhu X M, Moret R, Zabel H, Robinson I K, Vlieg E and Fleming R M 1990a *Phys. Rev.* B **42** 8791
Zhu X M, Zabel H, Robinson I K, Vlieg E, Dura J A and Flynn C P 1990b *Phys. Rev. Lett.* **65** 2692